ENGINYERIA ELECTRÒNICA ELÈCTRICA I AUTOMÀTICA

UNIVERSITAT ROVIRA I VIRGILI

Graduate Students Meeting on Electronics Engineering

Tarragona, June 29th and 30th, 2023

BOOK OF ABSTRACTS

IEEE

ENGINYERIA ELECTRÒNICA ELÈCTRICA I AUTOMÀTICA

UNIVERSITAT ROVIRA I VIRGILI

Graduate Students Meeting on Electronics Engineering

Tarragona June 29th and 30th, 2023

Program

Thursday, June 29th:

Sala de Graus ETSE

15.00 - Opening

15.10 – Keynote: Fernando Ávila Herrera (Globalfoundries, Dresden, Germany)

"High Voltage MOSFET Compact Models Challenges"

16.00 – Invited: Akash Bachhuka (Universitat Rovira i Virgili)

"TBD"

16.45 – Invited: Fatima Ezahra Annanouch (Universitat Rovira i Virgili)

"Atomically layered transition metal dichalcogenides nanosheets for NO2 and NH3 gas sensing application"

17.30 - Refreshment and Poster Session

Friday, June 30th:

Sala de Graus ETSE

9.00 - Keynote: Claudio Paoloni (Lancaster University, UK)

"Renaissance of Travelling Wave Tube Technology for sub-THz Applications"

10.00 – Invited: Kuntal Mandal ((Universitat Rovira i Virgili)

"Dynamical Modelling, Control and Design of Electric Vehicle for Performance Evaluation"

10.45 – Coffee Break and Poster Session

11:15 - Invited: Dalal Fadil ((Universitat Rovira i Virgili)

"Synthesis, characterization and device applications of 2D materials"

12:00 - Keynote: Stefania-Alexandra Iakab (Center for Mass Spectrometry and Optical Spectroscopy, Mannheim, Germany)

"Monitoring small molecules from 3D cell culture models using MALDI MSI"

13.00 – Closing and Lunch

Invited Contributions
Keynote Speakers

Stefania-Alexandra Iakab

Center for Mass Spectrometry and Optical Spectroscopy, Mannheim, Germany

Monitoring small molecules from 3D cell culture models using MALDI MSI

Organoids and spheroids are attractive 3D cell culture models because they mimic specific *in vivo* physiological conditions, can be developed from human cells, and contribute towards animal-free research. Their analysis brings light on cell-cell and cell-microenvironment molecular composition and interactions, which creates opportunities in cancer research and drug screening. However, 3D molecular characterization is required for a complete understanding of the molecular composition and chemical changes of the entire system. Our workflow enables studying cell-cell interactions, invasive cell migration, tumor progression, and other spatially relevant interactions within 3D cell culture models which could be monitored in 3D using MALDI-MS. We analyzed a colon cancer-fibroblast co-culture spheroid model, and were able to distinguish between cell type specific small molecules in an unbiased manner and high throughput. Therefore, our 3D technology could enable the identification of desirable markers for studying biological mechanisms typical to each cell type, which could lay the grounds for developing 3D-MSI based drug screenings.

Fernando Ávila Herrera

Globalfoundries, Dresden, Germany

High Voltage MOSFET Compact Models Challenges

High Voltage MOSFET Compact Models Challenges

Fernando Avila Herrera

Invited Paper

[1]GlobalFoundries, Dresden, 01109, Germany
Email: fernando.avilaherrera@globalfoundries.com

Abstract

High voltage (HV) MOSFETs require more care in the model development due to the high electric fields that are needed for the device operation. The history of the compact models is long-enough for devices with conventional low operation voltages but relatively short for HV devices. Here, we present a review of the compact models that are until today accepted as industry standards.

1. Introduction

It is quite common that a circuit consists of high and low voltage devices. Several applications requirements require that high-voltage circuits have to be controlled through operational low-power circuits. Due to this type of applications, the combined circuits are usually manufactured under the same technology, which includes low and high voltage devices in order to save fabrication cost.

Additionally, a short channel device is required to achieve high density integration of the circuits, causing the so called short-channel effects. Thin silicon thickness technologies are used to optimize the channel control. However, resistance cannot be avoided, especially for very thin-layer MOSFETs.

Several MOSFET structures have been developed to sustain high voltages, namely HV MOSFETs are required to manage the power of complete systems. Such optimization is done through the resistance increase of the drain region, typically obtained by enlarging the drain-region length and reducing the drain-doping concentration (Low Drain Doped MOSFET, LDMOS).

2. Compact Models for HV MOSFETs

Compact models for high-voltage MOSFETs incorporate the prediction of the unique characteristics exhibited by these devices. They can accurately model the high electric fields in drift regions, impact ionization phenomena, asymmetry of the capacitances, etc.

As today, only two compact models have obtained industry standardization: HiSIM_HV and BSIMBULK [1][2].

HiSIM_HV is an advanced compact model specifically designed for high voltage applications and was the first industry standard model for this category. BSIMBULK (former BSIM6) is a model mainly used for non-HV purposes but recently adapted to handle high power demands. Other topics have to be added on top of the core model, such as, aging, breakdown voltage, device architecture variations.

3. Conclusion

The acceleration of hybrid circuits handling low and high-power systems requires the use of devices that are capable to handle such power, and therefore the use of accurate models to predict their behavior. Just two models are widely accepted to perform spice simulations, HiSIM_HV and BSIMBULK [1][2]. These models are valid for bulk technologies only, however they are very likely to be extended to other MOSFETs with different gate architectures, such as FinFETs, gate-all-around, etc.

References

[1] HiSIM_HV 2.5.0 User's Manual, HiSIM Res. Center, Hiroshima Univ., Hiroshima, Japan, 2023.

[2] BSIM-BULK Technical Manual. (2023).

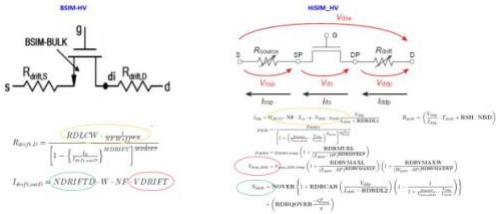

Fig.1 HiSIM_HV and BSIMBULK HV modeling principle.

Feature	HiSIM_HV 2.5	BSIM-BULK 107
Surface Potential	X	X
Asymmetric Capacitance	X	NA
Asymmetric resistance	X	X
Isub in drift region	X	X
Diode reverse recovery	X	NA
Self-Heating	X	X
5th Terminal (substrate)	X	NA

Invited Speakers

Kuntal Mandal

Group of Automatic Control and Industrial Electronics

Dynamical Modelling, Control and Design of Electric Vehicle for Performance Evaluation

The rekindling of interests in electric vehicles (EVs) for land transportation started due to rising demand of energy diversification, energy efficiency, and environmental protection. A general EV consists of many interconnected subsystems such as battery, converter, inverter, motor, and vehicle body along with overall control including thermal management, battery management system, auxiliary circuit, and other protection circuits. In this presentation, an overview will be given for the overall EV system and not just specific components. Then mathematical model of each subsystem is described using simple differential equations. The step-by-step design procedure of each subsystem is explained by algebraic equations. The control methodology will be discussed for optimizing energy, tracking, and vibration of the EV. Furthermore, the simulation results of the vehicle performance will be shown based on the general mathematical framework.

Fatima Ezahra Annanouch

Group of Microsystems Nanotechnologies for Chemical Analysis

Atomically layered transition metal dichalcogenides nanosheets for NO2 and NH3 gas sensing application

Inspired by the successful application of graphene based chemical gas sensors, 2D layered transition metal dichalcogenides (TMDs) materials have recently received immense attention and become the principal objective of many researches and gas sensing studies. They are characterized by their nanoscale thickness, layer-dependent band gap and large specific surface area (sheet-like structures), which enhances the “4S” sensor performances, i.e., sensitivity, selectivity, stability and speed. Among the 2D TMDs materials that have demonstrated their feasibility for gas sensing application, we found WS_2, MoS_2 and WSe_2, which have shown promising results towards NO_2, NH_3, H2S etc.

Dalal Fadil

Group of Microsystems Nanotechnologies for Chemical Analysis

Synthesis, characterization and device applications of 2D materials

Two dimensional materials like graphene have opened new perspective to other 2D materials such as transitional metal chalcogenide (TMC) and dichalcogenides (TMD), black phosphorus, and others. Thanks to the weak Van der Waals interactions between layers in bulk form, the majority of 2D materials can be synthesized by exfoliation. This method can provide high crystalline and good quality of material. However, exfoliation processing of 2D materials including reproducibility, the control of the thickness remains in some case a big challenge.

In this talk, it will be presented our methods of exfoliation of 2D materials by mechanical exfoliation and ecofriendly liquid phase exfoliation of different 2D materials and our results of their applications for optoelectronic, high frequency field effect transistors and gas sensor devices.

Akash Bachhuka

Group of Nanoelectronic and Photonic Systems

Nanoengineered surfaces for modulating cellular responses and sensing applications

The greatest challenge in the field of biomaterials is the understanding and prediction of long-term biological responses in patients receiving implantable materials. Reconstructing and detailing these mechanisms may allow for more targeted approaches and highlights how immune processes are amenable to manipulation by synthetic biomaterials. The interplay between plasma polymerized thin films in combination with surface nanotopography proved to be an important factor in cell-surface interaction. We demonstrated that the right combination of chemistry and nanotopography can be used to modulate cellular adhesion, collagen deposition, and macrophage polarization (the expression of pro-inflammatory and anti-inflammatory signals).

Furthermore, our surface engineering expertise was utilized to fabricate metal ion sensors and biosensors. We anticipate that future explorations in this field of research will facilitate the rational design of biomedical implants and devices with physicochemical surface characteristics tailored at the nanoscale that will enhance utility and function and improve clinical outcomes.

Invited Posters

Zouhair Haddi

Group of Microsystems Nanotechnologies for Chemical Analysis

Non-invasive and privacy preserving approaches for early detection of heart- and micturition-related diseases

Zouhair Haddi[1,2]*, Miquel Alfaras[1], Xavier Llauradó[1], Narcís Avellena[1], Eduard Llobet[2]
[1] NVISION Systems and Technologies SL, Barcelona, Spain
[2] Department d'Enginyeria Electronica, Universitat Rovira i Virgili, Tarragona, Spain

Aging is often related to a functional decline in physical and cognitive abilities leading/contributing to heart- and micturition-related diseases such as Diabetes mellitus and Congestive Heart Failure. In developed countries, the number of seniors living alone is growing rapidly. The current health care and management system relies on a reactive approach for the screening and diagnosis of those diseases (and others) putting extra burden on the seniors to launch the seek of assistance. Recently and especially during the past pandemic, many voices raised questioning the viability of the current system and encouraged the switch to a proactive model where screening and early detection of warning signs are conducted remotely and more importantly in a continuous manner. In this context, Health Smart Homes (HSH) and Health Monitoring Systems (HMS) are contributing to find out appropriate solutions to these challenges. HSH and HMS encompass several technologies including sensors, ICT, internet of things (IoT), internet of medical things (IoMT), artificial intelligence, decision support systems, digital twins, virtual twins, among others. In order to meet high acceptance and gain the stakeholders' trust, HSH and HMS have to fulfil several requirements such as the development/deployment of non-invasive and privacy-preserving technologies while processing the resulted data with trustworthy/ethical AI. In this event, we will disseminate the results of two on-going EU projects (EarlyCare and UPTAKE) and discuss how IoT gas/physiological sensors, as non-invasive and unobtrusive approach, could be deployed in some specific use cases to monitor activities of daily living and early detection of Diabetes mellitus and congestive heart failure warning signs.

Keywords: Gas sensors; Health Monitoring Systems; Non-invasive and unobtrusive technology; Artificial Intelligence.

ENGINYERIA ELECTRÒNICA ELÈCTRICA I AUTOMÀTICA

UNIVERSITAT ROVIRA I VIRGILI

Graduate Students Meeting on Electronics Engineering

Students Proceedings

Advanced metabolomics strategies to characterise the early life exposome

C. Guerrini[1,2], C. Torres[1], R. Giné[2], J. Badia[2], M. Vinaixa[2], N. Ramírez[1,2]

1 Institut d'Investigació Sanitària Pere Virgili (IISPV), Tarragona, Spain
2 Universitat Rovira i Virgili, Department of Electronic Engineering, Tarragona, Spain
email: camilla.guerrini@estudiants.urv.cat, tel.: 977256570

Abstract

Exposure to environmental pollutants during early life represents a significant threat to developing chronic and non-communicable diseases in adulthood. This work presents a wide-scope screening workflow which integrates high-resolution mass spectrometry and suspect screening analysis to fully identify the tobacco-related chemical exposome in urine as a case study for future clinical and epidemiological applications. The analysis of the first morning voids of 143 4-year-old children by Hermes tool (R software package) shows how curated MS/MS spectra facilitate the compounds' identification and biological interpretation. Statistical analysis demonstrates a correlation between tobacco-related compounds and socioeconomic aspects (education level and family income), and that 28% of non-exposed children have a level of 3-hydroxycotinine higher than the third quartile of the exposed children, thus demonstrating children's ubiquitous exposure to tobacco-specific toxicants.

Keywords: exposome, wide-scope screening, metabolomics, HRMS, Hermes

1. Introduction

Increasing evidence proves that causing oxidative stress and inflammation environmental chemical pollutants have a critical impact on human health, especially on children [1]. During the fundamental period for tissue organogenesis and functional development, toxic chemicals interfere with the development of systems, infant growth and evolution leading to irreversible damage [2]. Thus, characterising the early-life chemical exposome –all the chemical environmental stressors children are exposed to– is key to understanding the outbreak of later-life diseases. To date, the exposome community is facing two main gaps. Firstly, the traditional target approaches lack wide-scoped characterization in biofluids determining only a small number of exogenous pollutants. Secondly, the lack of information about the specific toxicity molecular mechanisms, which limits to link chemical exposure with health outcomes. non-targeted (NTA) and suspect-screening (SS) analysis are arising as new analytical strategies to characterise the chemical exposome [3,4]. In contrast to NTA, SS analysis focus on the determination of specific compounds of interest.

Here, we propose a workflow that integrates high-resolution mass spectrometry and suspect screening analysis to fully characterize the chemical exposome related to tobacco smoke exposure in children's urine. Among the numerous chemical compounds constituting the human exposome, exposure to tobacco smoke toxicants is ubiquitous and one of the major threats during early life [5]. The advanced data processing tools are based on the open-source package RHermes, which is a recent molecular formula-oriented optimization method of fragmentation data acquisition (MS/MS) developed in our research group [3].

2. Methodology

2.1. Sample

A cohort of 143 4-year-old children living in the area of Tarragona (Spain) was selected from the participants of the ECHOES project (Epigenetic and metabolic alterations associated to early childhood exposure to air pollution and its role in later life chronic disease), funded by La Caixa Foundation (LCF/PR/SR19/52540002). Children's morning voids were collected from October 2018 to June 2021. All parents or tutors/guardians signed an informed consent form approved by the Clinical Research Ethics Committee of the Institute of Health Research Pere Virgili (Ref. codes: 155/2017 and 086/2021) and filled out a general data questionnaire. The questionnaire collected socio-demographic and socioeconomic information including diet, physical activity, parental education level, monthly incomes, and exposure to tobacco smoke.

2.2. Sample extraction and metabolomics analysis

Fifty µL of each urine was extracted as reported in [6]. 2 µL of urine extracts were analysed with a Thermo Ultimate 3000 UHPLC system coupled with an Orbitrap ID-X Tribrid mass spectrometer (Thermo Fisher Scientific, Massachusetts, USA) in positive electrospray ionization mode (ESI+). The chromatographic separation was carried out using a Acquity UPLC BEH HILIC column at 25°C (2.1 mm × 150 mm, 1,7 µm) equipped with a guard column of the same chemistry (2.1 mm × 20 mm, 5 µm) both from Waters (Milford, MA, USA). The elution gradient was programmed using aqueous 50 mM ammonium acetate (eluent A) and acetonitrile (eluent B)

as mobile phases. The gradient elution started with an isocratic step of 100% of B (time 0-2 min), followed by a linear gradient to 100% of A (time 2-10 min), and finished at 100% of B (time 10-13 min. High-resolution MS1 and MS/MS spectra were acquired over the 60-900 m/z range. We used four fixed collision energies (10, 20, 30 and 40 V) for MS/MS acquisitions.

2.3. Data processing and statistical analysis

2.3.1. XCMS and statistical analysis

The workflow for LC-MS data processing was adapted from Vinaixa et al. [7]. Raw MS1 files were converted into mzML format using MSConvert software from Proteowizard [8] and were processed by the XCMS package (version 3.20.0) using R software environment (v4.2.0).

The two-dimensional matrix of 25716 features was filtered in a matrix with 937 statistically relevant based on ANOVA (p-value < 0.05 and fold change > 1.5). All statistical analyses (t-test, PCA, correlations) were performed using R software to associate the metadata with the identification results.

2.3.2. Suspect Screening Analysis based on Hermes

RHermes [3] (open-source R package) is a recent molecular formula-oriented optimisation method for tandem mass spectrometry. Hermes creates accurate inclusion lists (IL) with the aim of increasing mass spectral similarity scoring and identification rates.

Based on interrogating directly raw MS with the most relevant metabolic and exposome databases (e.g., Human Metabolome Data Base, LipidMaps, PubChemLite for Exposomics), the computing of theoretical isotopic patterns and grouping points with the same m/z by density into retention time range and their chromatographic elution profile, Hermes produces sample-specific and non-redundant precursor ions grouped in an IL. The IL of tobacco exposure included 117 specific compounds and was achieved from the THS database [9].

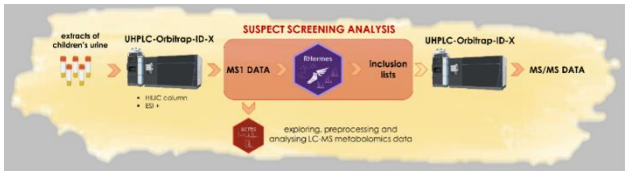

Fig. 1. Metabolomics workflow proposed in this work.

3. Results

In our study, suspect screening LC-MS/MS based on Hermes was performed to determine the metabolic and exposome profile of the urine. The population includes two groups which are representative of Spanish children in terms of socioeconomic vulnerability and from urban, suburban and rural areas: no/minimal tobacco smoke exposure (92 children, 64%) and mixed SHS and THS exposure (51 children, 36%).

We identified some tobacco metabolites with higher mass spectral similarity as shown in Figure 2 for the 3-hydroxycotinine, which is a metabolite of nicotine and an excellent indicator of exposure to tobacco smoke.

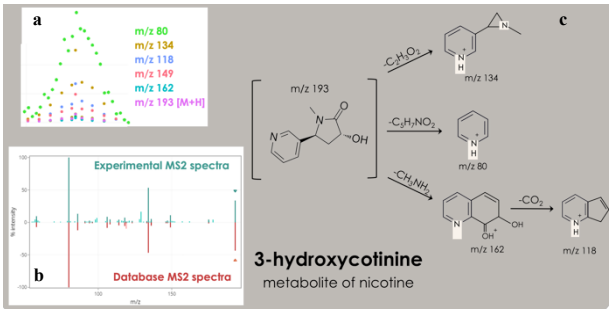

Fig. 2. (a) fragment ions from continuous MS/MS scans are grouped according to their m/z (b) loose peak-picking algorithm groups the peaks according to their elution profiles to form curated MS/MS spectra (c) principal fragments of 3-hydroxycotinine.

From the statistical analysis, we observed an association between childhood exposure (3-hydroxycotinine) and familiar incomes and parents' studies (*p-value* adjusted for *"False Discovery Rate"* < 0.05, Figure 3): parent's studies and socioeconomic status are inversely related to exposition to tobacco compounds. Moreover, the distribution of 3-hydroxycotinine reveals that 28% of non-exposed children have a higher relative concentration of tobacco toxicants biomarkers than the third quartile of exposed ones.

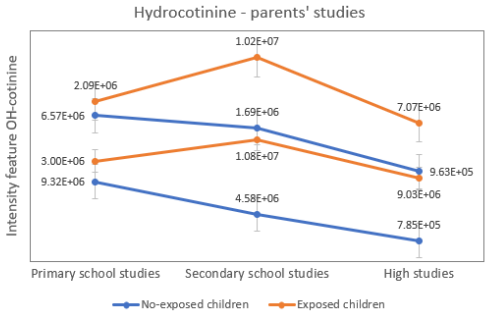

Fig. 3. Parental smoking decreases when the education level is high

7. Conclusions

Our study shows the advantage of using a suspect screening workflow based on Hermes. Thanks to the increased specificity of MS2 scans, improved mass spectral similarity scoring exogenous compounds were identified with more confidence. The preliminary results confirm the impact of tobacco smoke exposure on children and the necessity of future political decisions.

References

[1] Gluckman PD, Hanson MA, Cooper C, Thornburg KL. Effect of in utero and early-life conditions on adult health and disease. New England Journal of Medicine 2008;359(1):61-73. DOI: 10.1056/NEJMra0708473

[2] WHO Air pollution and Child Helth. Prescribing clean air, 2018

[3] Giné R, Capellades J, Badia JM, et al. HERMES: a molecular formula-oriented method to target the metabolome. 2021:2021.03.08.434466. DOI: 10.1101/2021.03.08.434466.

[4] Schymanski EL, Kondic T, Neumann S, Thiessen PA, Zhang J, Bolton EE. Empowering large chemical knowledge bases for exposomics:

PubChemLite meets MetFrag. Journal of cheminformatics 2021;13(1):19-19. DOI: 10.1186/s13321-021-00489-0. [7] (IARC), I.A.f.R.o. C.
[5] IARC Monograph vol.83 Tobacco Smoke and Involuntary Smoking; 2004
[6] Southam, A. D., Haglington, L. D., Najdekr, L., Jankevics, A., Weber, R. J. M., & Dunn, W. B. (2020). Assessment of human plasma and urine sample preparation for reproducible and high-throughput UHPLC-MS clinical metabolic phenotyping. Analyst, 145(20), 6511–6523. https://doi.org/10.1039/d0an01319f
[7] Vinaixa, M.; Samino, S.; Saez, I.; Duran, J.; Guinovart, J.J.; Yanes, O. A Guideline to Univariate Statistical Analysis for LC/MS-Based Untargeted Metabolomics-Derived Data. Metabolites 2012, 2, 775–795, doi:10.3390/metabo2040775.
[8] Holman, J.D.; Tabb, D.L.; Mallick, P. Employing ProteoWizard to convert raw mass spectrometry data. Curr. Protoc. Bioinforma. 2014, 46:13.24.1, doi:10.1002/0471250953.bi1324s46.
[9] (Thirdhand smoke database, https://zenodo.org/record/5395357)

An Emerging TMDC $PtSe_2$ Based Gas Sensor for NO_2 Sensing

Mubdiul Islam Rizu, Dalal Fadil, Eduard Llobet

Minos Research Group. Universitat Rovira i Virgili. Av. Països Catalans 26, 43007 Tarragona, Spain.

Abstract

Beyond other 2D layered nanomaterials, $PtSe_2$ is a Transition Metal Dichalcogenide (TMDC) comprising high surface-to-volume ratio, superior carrier mobility and having potential for sensing toxic gases. We have designed and fabricated chemiresistive gas sensor for NO_2 sensing by mechanically exfoliated $PtSe_2$ into few layered flakes and transferred on the top of gold contacts by using a mask aligner. The primary results reveal very high response of 862.81% for 60 ppm concentration of NO_2 at room temperature. This result clearly indicates that $PtSe_2$ holds promise for toxic gas detection and shows good prospects for its manufacturing by the semiconductor industry embracing CMOS compatible methods.

1. Introduction

In the contemporary 2D nanomaterial research, the group-10 TMDC $PtSe_2$ exhibits unprecedented physical and chemical properties such as requiring low temperature synthesis methods, high charge-carrier mobilities and long-term air stability [1]. Due to its exceptional layer-dependent properties, a phase transition from metal-to-semiconductor occurs as the thickness is reduced from bulk to monolayer [2]. Furthermore, theoretical as well as experimental studies on $PtSe_2$ have demonstrated its exceptional sensing ability toward toxic gas detection [3]. This type of gas sensor typically determines the change in the electrical properties of $PtSe_2$ channels when they are subject to different gaseous analytes.

2. Sample Preparation

Our chemiresistive gas sensor was fabricated on the silicon substrate. Using photolithography, the contacts were patterned and fabricated. For the transfer of the $PtSe_2$ flake in between the contacts, we utilized the mask aligner Karl Suss MJB4 as shown in figure 2.1. First, $PtSe_2$ crystal was mechanically exfoliated using Magic scotch tape. Then, the $PtSe_2$ flakes were transferred to a PDMS film held by a 4 by 4-inch glass. This glass is attached to the mask aligner holder. The SiO_2/Si substrate with the prepatterned contacts is placed in the chuck. Finally, the alignment and transfer were done using the mask aligner and then observed under the optical microscope [4].

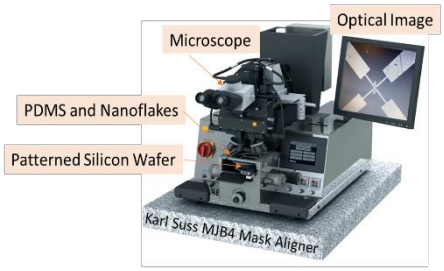

Fig 2.1. Transfer technic of $PtSe_2$ flake using mask aligner.

3. Device Characterization

After transferring the $PtSe_2$ flake in the prepatterned contacts over the substrate, Pt wire bonding between Printed Circuit Board (PCB) and contacts has been established to complete the sensor circuit as shown in Figure 3.1.

Fig 3.1. $PtSe_2$ Sensor Bonded to PCB.

The surface morphology of $PtSe_2$ channel was examined by Field Emission Scanning Electron Microscopy (FESEM) shown in figure 3.2. The flake size was measured as 79.60 µm × 22.50 µm which is highly favorable to adsorb the gas in the channel.

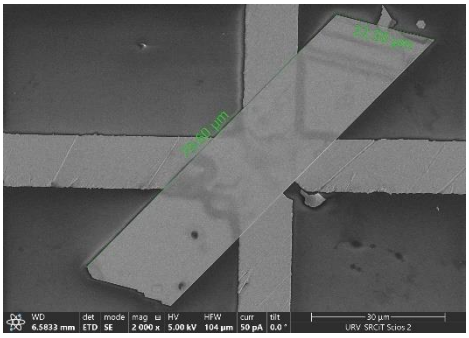

Fig 3.2. FESEM of a mechanically exfoliated $PtSe_2$ flake.

The Raman spectroscopy study was performed using 633 nm laser excitation to confirm the formation of $PtSe_2$ shown in figure 3.3. Two prominent peaks at 176 cm^{-1} and 206.7 cm^{-1} corresponding to the E_g in-plane vibration Raman active mode and the A_{1g} out-of-plane vibration modes of Se atoms respectively.

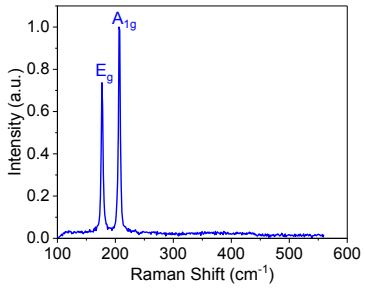

Figure 3.3. Raman Spectrum of $PtSe_2$ flake.

As we can observe figure 3.4, the Energy Dispersive Spectroscopy (EDS) analysis of exfoliated $PtSe_2$ deposited on SiO_2/Si substrate shows a strong presence of Pt and Se with quasi free impurity. The small Si peaks reconfirm the suspension of the material.

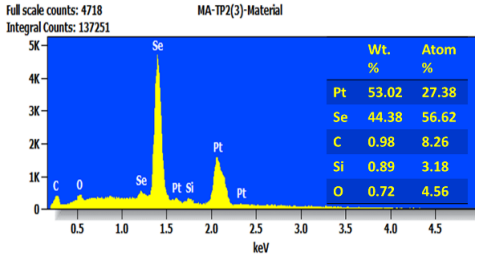

Figure 3.4. EDS Spectrum of $PtSe_2$ flake.

From the Atomic Force Microscopy (AFM) analysis, the gap between the substrate and the suspended $PtSe_2$ flake was found 79.3 nm (figure 3.5). The surface roughness is noticeable as the mean roughness was found 24.28 nm.

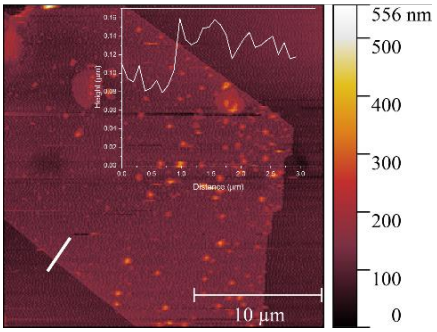

Figure 3.5. AFM Image of Exfoliated $PtSe_2$ flake.

Before going for gas sensing measurement, it is important to assure whether the sensing channel is well conducting or not. Figure 3.6 shows the I-V characteristics where we can find the dominance of linear behaviour of our sensor up to 1.6 V and then it started saturating. After 2.2 V, the sensor reached its breakdown point. The resistance was calculated as 34.32 **Ω.**

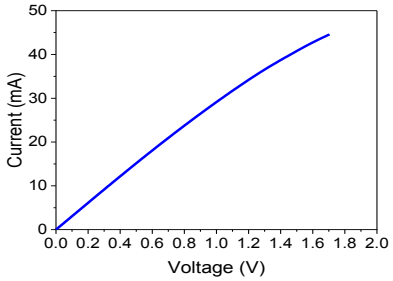

Figure 3.6. I-V Characteristics $PtSe_2$ Chemiresistive Sensor.

4. Result and Discussion

Here the sensing mechanism is attributed to the charge transfer between NO_2 gas and $PtSe_2$ sensing material. The unpaired electron in NO_2 withdraw electron from $PtSe_2$ which results in decreasing electron concentration in the conduction band of the $PtSe_2$. Our $PtSe_2$ sensor was exposed to 60 ppm NO_2 at room temperature. The sensor response was calculated by the resistance of the device before and after the exposure of NO_2 gas. Our sensor was able to give a response of 862.81%, which is highly commendable. Figure 4.1 also indicates the quick recovery time of our sensor which is an essential figure of merit for gas sensing performance.

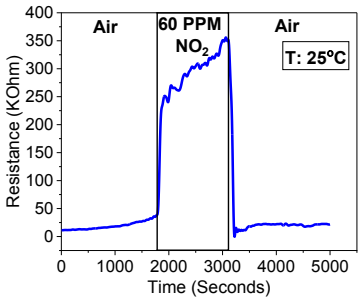

Figure 4.1. $PtSe_2$ Sensor response for 60 ppm NO_2.

5. Conclusion

Our $PtSe_2$ chemiresistive gas sensor has shown promising behaviour towards NO_2 gas sensing at room temperature. In near future $PtSe_2$ channel-based FET gas sensor will be designed and fabricated. Furthermore, this sensor will be characterized from DC to high frequency range to test its performance as a microwave gas sensor for the new generation of 5G enabled IoT devices as well as unattended gas sensing networks.

References

[1] Cao, Banglin, et al. "Recent progress in van der Waals 2D PtSe2." Nanotechnology 32.41 (2021): 412001.

[2] Ciarrocchi, Alberto, et al. "Thickness-modulated metal-to-semiconductor transformation in a transition metal dichalcogenide." Nature communications 9.1 (2018): 919.

[3] Sajjad, Muhammad, et al. "Superior gas sensing properties of monolayer PtSe2." (2016).

[4] Saenz, Gustavo A., Dalal Fadil, and Anupama B. Kaul. "Analysis of multilayer black phosphorus for photodetector applications." Image Sensing Technologies: Materials, Devices, Systems, and Applications IV. Vol. 10209. SPIE, 2017.

Modeling Approach for Schottky Barrier Field-Effect Transistors at Deep Cryogenic Temperatures

Christian Roemer, Nadine Dersch, Ghader Darbandy, Mike Schwarz, Benjamín Iñíguez and Alexander Kloes

***Abstract*—This paper demonstrates the approach for a closed-form and physics-based compact model that can be used to calculate the charge carrier injection current of a Schottky barrier field-effect transistor at deep cryogenic temperatures. The basic equations of the model are shown, including an adjusted expression for the supply function at deep cryogenic temperatures, as well as an empirical addition in order to describe resonant tunneling effects. Finally, the compact model is compared to a set of measurements.**

***Index Terms*—SBFET, cryogenic, compact modeling, closed-form, Schottky barrier, Field emission, tunneling current**

I. Introduction

THE field of transistors used in deep cryogenic temperature environment still is a niche problem, however, with increasing technological areas (e.g. quantum computing) the demand for electronic devices in this temperature environment is also raising [1]. A promising candidate for electronics application in deep cryogenic environment is the Schottky barrier field-effect transistor (SBFET), which controls the current flow by charge carrier injection over the device's Schottky barriers [1]–[4]. In this paper, an overview of the work performed in [5] is given. Section II describes the modeling approach with the most important equations and Sec. III shows a model fit to measurements. Finally, in Sec. IV, a conclusion of the work is given.

II. Modeling Approach

The compact modeling approach presented in this paper is similar to the approach shown in [5] and is made to calculate the DC current flowing through a double-gate (DG) structure SBFET as shown in Fig. 1a.

In order to calculate the field emission (FE) current that is injected at the device's Schottky barrier, a potential model is needed, which is used for a potential and band diagram reconstruction along the device's channel. With such a model, the band diagram at the Schottky barriers (shown for example in Fig. 1b) can be reconstructed and important parameters for the following calculations can be extracted. The used potential model is described in [2], [5]–[7], but is beyond the scope of this work.

The FE current calculation is done by using the Tsu-Esaki formula, as

$$J_{\mathrm{FE,n}} = \frac{q \cdot m^*}{2\pi^2\hbar^3} \cdot B_{\mathrm{PAT}} \cdot \int_{E_{\mathrm{C,min}}}^{E_{\mathrm{fs}}} T(\mathcal{E}) \cdot N(\mathcal{E}) \cdot d\mathcal{E}\,, \qquad (1)$$

where q is the elementary charge, $\hbar$ is the reduced Planck's constant and m^* is the charge carrier's effective tunnel mass given as $m_{\mathrm{n}} \cdot m_0$ for electrons or $m_{\mathrm{p}} \cdot m_0$ for holes and used as fitting parameter [8]. The parameter B_{PAT} is used

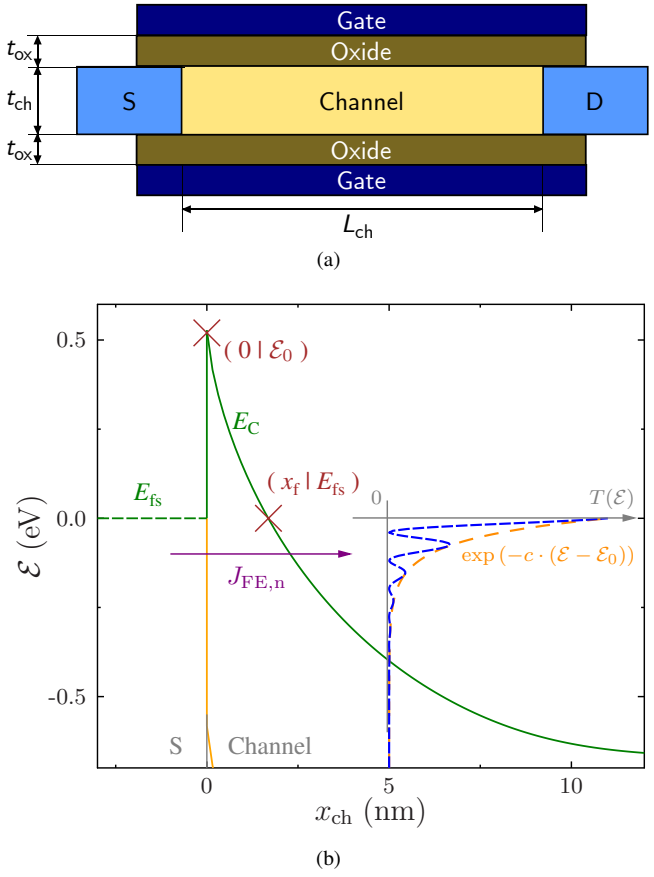

Fig. 1. (a) Schematic cross-section of the DG SBFET with the relevant geometric parameters which is used for compact modeling. (b) band diagram of the source side Schottky barrier during a device's on-state, with the important parameters for the current calculation. The right-hand side plot shows tunneling probability from (3) vs. energy.

This project is funded by a grant from TH Mittelhessen University of Applied Sciences, Giessen, Germany. We acknowledge the support by Yi Han and Qing-Tai Zhao from Peter-Grünberg-Institute (PGI 9), Forschungszentrum Jülich, Jülich, Germany.

Christian Roemer is with NanoP, TH Mittelhessen - University of Applied Sciences, Giessen, Germany and DEEEA, Universitat Rovira i Virgili, Tarragona, Spain (e-mail: christian.roemer@ei.thm.de). Nadine Dersch, Ghader Darbandy, Mike Schwarz and Alexander Kloes are with NanoP, TH Mittelhessen - University of Applied Sciences, Giessen, Germany. Benjamín Iñíguez is with DEEEA, Universitat Rovira i Virgili, Tarragona, Spain.

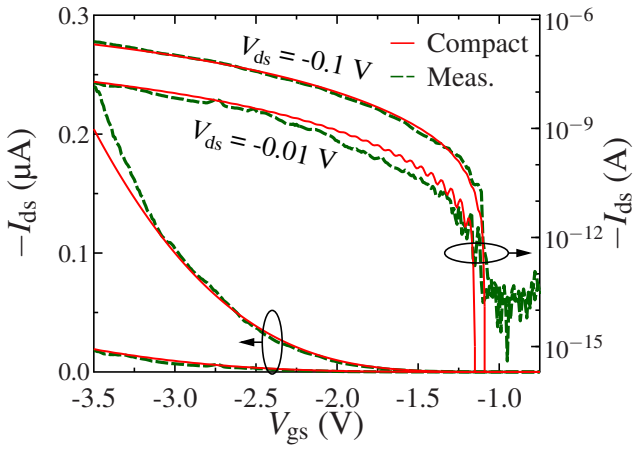

Fig. 2. Device measurements (green dashed lines) compared to the compact model results (red solid lines), shown as transfer characteristics in linear and logarithmic scale. The device's channel length is 70 nm and the temperature 5.3 K. The measurements are taken from [1].

to include the expected tunneling current reduction caused by the absence of phonon scattering events and therefore, the missing possibility for carriers to change their $\vec{k}$-vector at deep cryogenic temperatures [5], [9]. In the compact model, B_{PAT} is used as a fitting parameter in a range of zero to one, but much smaller than one [5].

$N(\mathcal{E})$ is the supply function, which is expressed by

$$N(\mathcal{E}) = \int_0^\infty \left(f_{\mathrm{s}}(\mathcal{E}_{\mathrm{tot}}) - f_{\mathrm{d}}(\mathcal{E}_{\mathrm{tot}})\right) \cdot d\mathcal{E}_\rho \,, \tag{2}$$

with f_{s} and f_{d} as the Fermi distribution function in source and drain region, respectively, as well as the charge carrier's total energy $\mathcal{E}_{\mathrm{tot}} = \mathcal{E} + \mathcal{E}_\rho$ separated in its longitudinal $\mathcal{E}$ and transversal $\mathcal{E}_\rho$ energy components [8], [10]. As it has been demonstrated in [5], the supply function for a temperature of $\vartheta \to 0\,\mathrm{K}$ can be approximated by $E_{\mathrm{fs}} - \mathcal{E}$, which is a huge simplification of (1).

$T(\mathcal{E})$ is the tunneling probability, given as

$$T(\mathcal{E}) = \exp\left(-c \cdot (\mathcal{E}_0 - \mathcal{E})\right) \cdot \sin^2\left(\omega_{\mathrm{E}} \cdot \mathcal{E} + \varphi_0\right) . \tag{3}$$

The expression of the tunneling probability is separated into two main terms. The exponential term is an approximation of the triangular Wentzel-Kramers-Brillouin (WKB) approach, where c is calculated by this triangular WKB at position x_{f}, according to [2]. The sinusoidal part is an empirical addition that shall include the resonant tunneling effect into the compact model, where the fitting parameters ω_{E} and φ_0 are used to control the frequency and phase of the resonant tunneling oscillations [5]. The contributions of (3) are schematically shown in Fig. 1b.

Using (3) and the solution of (2) in (1) leads to an analytically solvable integral that can be used to obtain the device's source side injection current density. In addition, the current balancing model of [2], [5] is used and with the device's geometric parameter a total drain current I_{d} is calculated.

III. Model Results and Verification

Figure 2 shows the results of a compact model fit to the measured ultra-thin body and buried oxide SOI SBFETs [1], [5]. In general, the compact model shows a good agreement to the measurements. The curves calculated by the compact model fit to the measurements in most regions and the oscillations, contributed by the sinusoidal part of (3), are also fitting to the measured oscillations for $V_{\mathrm{ds}} = -0.01\,\mathrm{V}$.

However, there are still some discrepancies between measurements and compact model. The model's slope is slightly too steep, compared to the measured data, which is most likely be caused by the presence of band tail states contributing to the off-current [4]. In addition, the oscillations of the $V_{\mathrm{ds}} = -0.1\,\mathrm{V}$ curves are more pronounced in the measured data.

IV. Conclusion

A physics-based carrier injection compact model for SBFETs at deep cryogenic temperatures is derived in this paper. The verification is done by a comparison to measurements. It could be verified that the compact model is able to capture and describe the important transport mechanisms in the given temperature and bias range. There is also room for improvement for the compact model, regarding the inclusion of second order effects like band tail states.

References

[1] Y. Han, J. Sun, F. Xi, J.-H. Bae, D. Grützmacher, and Q.-T. Zhao, "Cryogenic characteristics of UTBB SOI Schottky-barrier MOSFETs," *Solid-State Electronics*, vol. 194, p. 108351, Aug. 2022.

[2] C. Roemer, G. Darbandy, M. Schwarz, J. Trommer, A. Heinzig, T. Mikolajick, W. M. Weber, B. Iniguez, and A. Kloes, "Physics-based DC compact modeling of Schottky barrier and reconfigurable field-effect transistors," *IEEE Journal of the Electron Devices Society*, vol. 10, pp. 416–423, 2022.

[3] M. Schwarz, L. E. Calvet, J. P. Snyder, T. Krauss, U. Schwalke, and A. Kloes, "On the physical behavior of cryogenic IV and III–V Schottky barrier MOSFET devices," *IEEE Transactions on Electron Devices*, vol. 64, no. 9, pp. 3808–3815, Sep. 2017.

[4] Y. Han, J. Sun, B. Richstein, F. Allibert, I. Radu, J.-H. Bae, D. Grutzmacher, J. Knoch, and Q.-T. Zhao, "Steep switching Si nanowire p-FETs with dopant segregated silicide source/drain at cryogenic temperature," *IEEE Electron Device Letters*, pp. 1–1, 2022.

[5] C. Roemer, N. Dersch, G. Darbandy, M. Schwarz, Y. Han, Q.-T. Zhao, B. Iñíguez, and A. Kloes, "Compact modeling of Schottky barrier field-effect transistors at deep cryogenic temperatures," *Solid-State Electronics*, p. 108686, Jun. 2023.

[6] M. Schwarz, T. Holtij, A. Kloes, and B. Iniguez, "Analytical compact modeling framework for the 2D electrostatics in lightly doped double-gate MOSFETs," *Solid-State Electronics*, vol. 69, pp. 72–84, Mar. 2012.

[7] M. Graef, T. Holtij, F. Hain, A. Kloes, and B. Iniguez, "Improved analytical potential modeling in double-gate tunnel-FETs," in *2014 Proceedings of the 21st International Conference Mixed Design of Integrated Circuits and Systems (MIXDES)*. IEEE, Jun. 2014.

[8] F. Horst, A. Farokhnejad, Q.-T. Zhao, B. Iniguez, and A. Kloes, "2-D physics-based compact DC modeling of double-gate tunnel-FETs," *IEEE Transactions on Electron Devices*, vol. 66, no. 1, pp. 132–138, Jan. 2019.

[9] R. B. Floyd and D. G. Walmsley, "Tunnelling conductance of clean and doped Al-I-Pb junctions," *Journal of Physics C: Solid State Physics*, vol. 11, no. 22, pp. 4601–4614, Nov. 1978.

[10] A. Gehring, "Simulation of tunneling in semiconductor devices," Ph.D. dissertation, Technische Universität Wien, 2003. [Online]. Available: https://resolver.obvsg.at/urn:nbn:at:at-ubtuw:1-12051

Carbazole-Based Conjugated Molecules as Self-Assembled Hole Transporting Monolayers for Inverted Perovskite Solar Cells

Dora A. González[1,2], Carlos E. Puerto Galvis[1], Wenhui Li[1], Maria Mendéz[1], Ece Aktas[1,3], Eugenia Martínez-Ferrero[1] and Emilio Palomares,[1,4]*

[1]*Institute of Chemical Research of Catalonia (ICIQ-BIST). Avda. Països Catalans 16, 43007, Tarragona, Spain.*

[2]*Department of Electric, Electronic and Automatic Engineering, Universitat Rovira i Virgili, Avda. Països Catalans 26, 43007, Tarragona, Spain.*

[3] *Current address: Department of Chemical, Materials and Production Engineering, University of Naples Federico II, Piazzale Tecchio 80, 80125 Fuorigrotta, Italy.*

[4]*ICREA. Passeig Lluís Companys 23,08010, Barcelona, Spain.*

Email of corresponding authors:

*epalomares@iciq.es

emartinez@iciq.es

dagonzalez@iciq.es

Abstract

Self-assembled monolayers (SAMs) are a potential candidate as hole transport materials (HTMs) for inverted perovskite solar cells (iPSCs) due to their high stability achieved and their low-cost fabrication procedures. Here we report three new SAMs (**SAM1, SAM2 and SAM3**) based on a carbazole core by an efficient synthetic procedure. SAMs were designed and synthesized featuring special groups to study and understand the effects and interactions between SAM/perovskite interface, which plays a fundamental role. The resulting device showed a champion efficiency of 18.9 %, 17.6 % and 17.5 % for SAM1, SAM 2 and SAM3 respectively.

Introduction

Over the last decade, perovskite solar cells have been improved, in a very short period, from 3.8% of efficiency to 25.7 % for regular configuration (n-i-p) and 24.2 % for inverted configuration (p-i-n) [1], [2]. This huge progress in the device performance has been achieved thanks to the perovskite composition and charge transporting layers among others. Among them, charge transporting materials, including electron transporting material (ETM) and hole transporting material (HTM), play a key role to achieve such efficiencies [3]. Particularly, the synthesis and design of HTMs have become an important topic in the perovskite research community [4]–[6]. Recently, a new family of HTM known as SAMs had attracted tremendous attention for use as hole selective contact in inverted perovskite solar cells (iPSCs) [7], [8]. SAM molecules present several advantages in comparison to the widely used poly[bis(4-phenyl)(2,4,6-trimethylphenyl)amine] (PTAA) polymer, for instance in terms of cost, reproducibility and stability [8], [9]. Furthermore, SAM-based iPSC has achieved over 24 % efficiency [10], indicating that SAMs are promising as hole selective contacts for high-performance devices. SAM molecules are mainly composed of three different parts i) the anchoring groups, such as the phosphonic acid, silane, and carboxyl acid groups, ii) the linker groups with the commonly used alkyl chains or conjugated benzenes and iii) the functional groups like amines, thiols, or carbazole [11]. The anchoring groups chemically bond with ITO to form a strong and uniform monolayer. The

linker groups determine the charge transport properties and molecular packing, as well as the geometry and contact angle. The functional groups interact directly with the perovskite layer, improving the surface coverage and inducing changes in the surface properties [4], [11]. Recently, it has showed by introducing other well-known HTM groups to form a SAM can have a positive impact on the performance of the devices [12]. In particular, the carbazole core for the HTMs is widely adapted in the synthesis of new materials for solar cells. The first use of carbazole core as an anchoring group of the SAMs was implemented in 2018 by Artiom et al. where above 17 % PCE can reach using a small amount of SAM as a dopant-free hole selective contact [7]. Amran et al. integrated new two SAMs (MeO-2PACz and 2PACz) which were designed to create an energetically aligned interface for three different perovskite compositions, allowing for reduced non-radiative recombination at the interface between the perovskite/contact layer, and reaching efficiencies of up to 20 %. The results highlight that carbazole derivatives can combine all necessary features for lossless interfaces and are thus a class of material for future chemical engineering of high-performance hole-selective contacts [8]. E. Yalcin et al. demonstrated the influence of the SAMs on the surface of ITO and improved perovskite performance [9]. After these, several studies undertaken on SAMs have been already studied previously by other authors [6], [13]–[16]. In this work, we focused on the analysis of the interfaces to study the interaction between ITO/SAM and perovskite/SAMs in the iPSCs. Additionally, here it is reported the chemical and photophysical properties of the new three SAMs by using different characterization techniques.

Results and Discussion

Based on the design principles of self-assembled molecules, three new SAM molecules were designed and synthesized with the carboxylic acid (-COOH) as an anchoring group, the phenyl or biphenyl moieties as a linker, and different substituted carbazole-core as a functional. See **Scheme 1** for the synthesis pathway of **SAM1**, **SAM2**, and **SAM3**. The structures of the synthesized compounds were confirmed by means of ^{1}H and ^{13}C NMR spectroscopy. Then, we compared the photovoltaic performance of the different SAMs in iPSCs. The as-synthesized SAMs were used as HTM in iPSC based on a triple cation perovskite $(Cs_{0.05}(FA_{0.85}MA_{0.15})_{0.95}Pb(I_{0.85}Br_{0.15})_3$ onwards labeled as CsFAMA) [15], [17].

We employed the following device structure: ITO//SAMs//CsFAMA//$PCBM_{61}$//BCP//Ag, shown in Figure 1 (b). In addition, the energetic alignment of the SAMs and CsFAMA are illustrated in Figure 1 (a), where the energy level for EADR03 (as a reference) and CsFAMA were obtained from the literature [13] and the values are referenced to the vacuum level, while the energy levels of SAM1, SAM2 and SAM3 were estimated using absorption, photoluminescence and cyclic voltammetry (see Figure 1 (c) and (d).

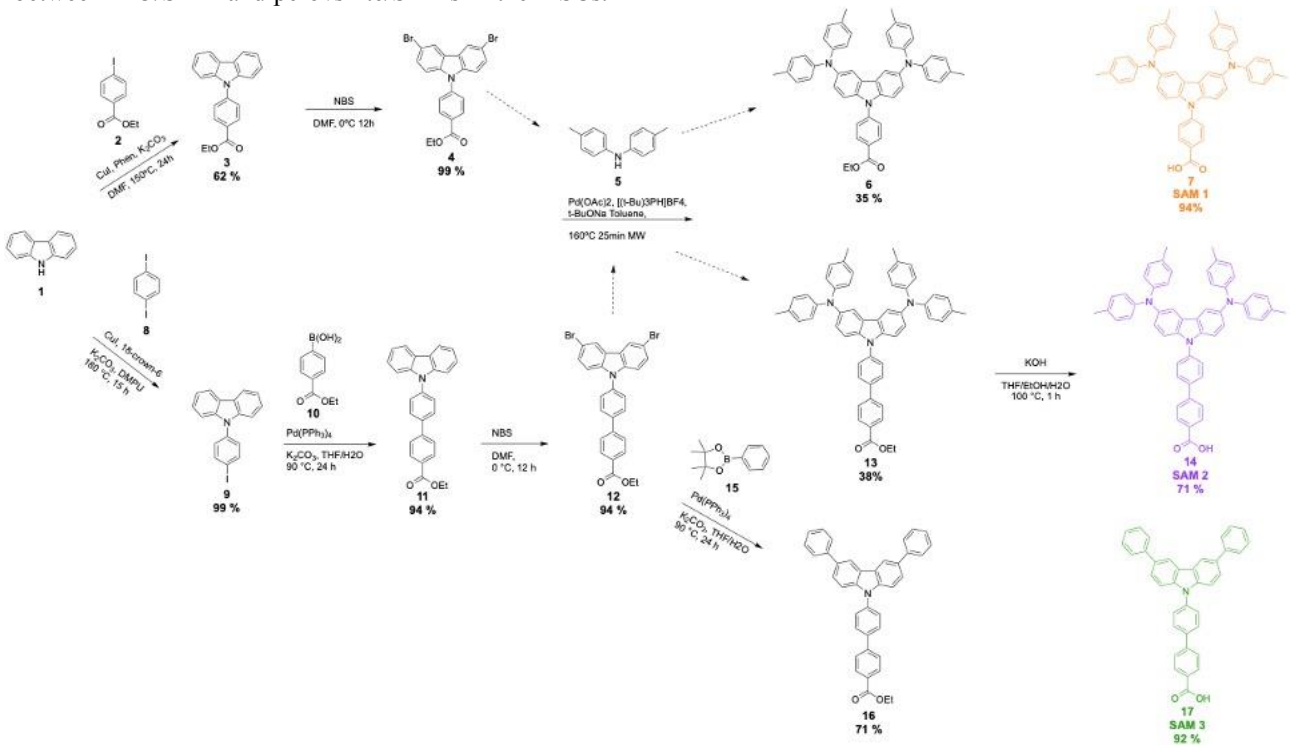

Scheme 1. Synthesis pathway of SAM molecules used as hole-transporting materials in iPSCs.

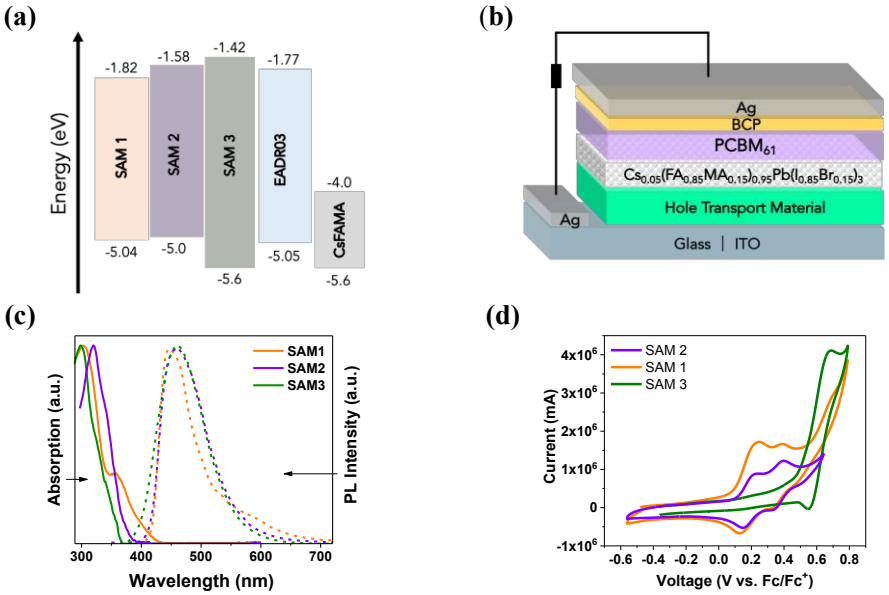

Figure 1. (a) The energy levels of the SAMs, EADR03 and perovskite, **(b)** Architecture of the p-i-n device used in this work, **(c)** UV-vis Absorption and Emission Spectra of conjugated SAMs in DCM and **(d)** Cyclic voltammetry results of conjugated SAMs in the supporting electrolyte (TBAPF6 in dichloromethane, DCM), measured using ferrocene (Fc/Fc+) as an internal reference.

The UV-Visible absorption and photoluminescence (PL) spectra were recorded for the three molecules in solution (10^{-5} M in dichloromethane) see **Figure 1c**. All of them show a wide absorption band in the UV part of the spectrum ranging from 290 to 400 nm which are assigned to the well known π-π* transitions [7]. The maximum absorption value (λ_{max}) was used to obtain the PL emission spectra, showing a wide emission band with a maximum of 452 nm for **SAM1**, 446 nm for **SAM2** and 470 nm for **SAM3**. The optical gap LUMO of SAMs was estimated from the absorption edge wavelength using UV-vis measurements [18].

Cyclic voltammetry was performed to calculate the HOMO values (see **Fig. 1d**) [19]. **SAM1** and **SAM2** exhibit two reversible oxidation waves assigned to the extraction, mainly, from the di-p-tolylamine groups, while **SAM3** shows only one wave due to carbazole core. However, the introduction of phenyl groups in **SAM3** leads to a deeper HOMO value of -5.6 eV compared to -5.04 eV for **SAM1** and -5.0 eV for **SAM2**. In accordance with the results, the energy levels of the new SAMs are suitable with respect to the perovskite energy levels. The surface wettability of the ITO-coated substrates was investigated by measuring the contact angle after homogenously covering with the SAMs solution by spinning method.

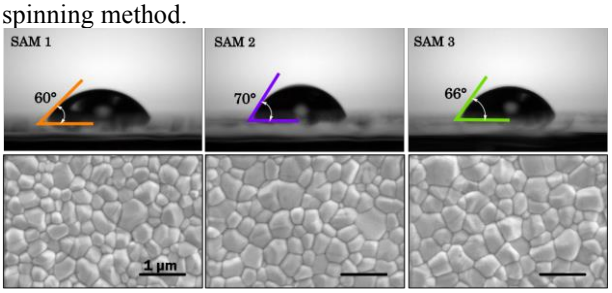

Figure 2. Contact angle measurements on the different HTMs surfaces and the FESEM top view of perovskite films deposited on ITO/SAM1, ITO/SAM2 and ITO/SAM3.

The contact angles of water on SAM1, SAM2 and SAM3 are estimated at 60°, 70° and 66°, respectively, which shows a higher hydrophobicity character in comparison to EADR03 estimated at 50° (see Fig. 2 top-images). Furthermore, the contact angle of bare ITO is estimated at 55°, indicating that SAMs are well covered onto ITO and enhance the surface energy and the spread of perovskite solution. We employed field emission scanning electron microscopy (FESEM) to corroborate this effect on the morphology of the perovskite layer, as shown in Figure 2 bottom images. To confirm the surface modification on the ITO by SAM molecules, X-ray photoelectron spectroscopy (XPS) was used to examine the atomic bonds of SAMs on the metal oxide surface (see **Figure 3**). The C1s spectra were decomposed into 3 peaks assigned to C–C or C–H (285 eV approx.), C–O (286 eV approx.) and COOCH (289 eV approx.) bonds. The N1s spectra show the same peak position around 400 eV for all the SAMs assigned to C–N bond, which is not observed on ITO. This indicates the formation of the self-assembled monolayer on the ITO.

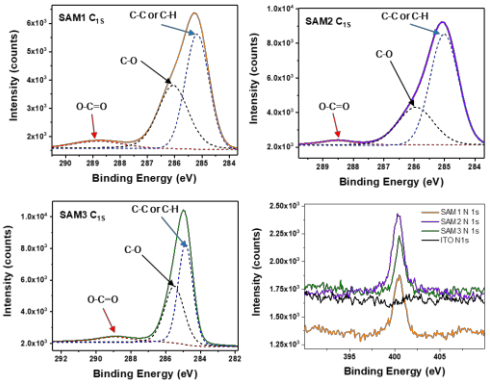

Figure 3. X-ray photoelectron spectroscopy of C1s and N1s for SAMs on the treated ITO

To evaluate the photovoltaic performance of three SAM molecules as HTM in iPSCs, a devices based on

CsFAMA with a configuration of ITO//SAMs// CsFAMA//$PCBM_{61}$//BCP//Ag. The CsFAMA was prepared by two steps anti-solvent method following our previous report[13]

In brief, the SAMs were deposited onto the ITO substrate by spin-coating method, and the layer was optimezed to obtain the best performance for each SAM under an inert atmosphere. Figure 4 displays the current density voltage (*J-V*) in forward (fwd) and reverse (rev) scans and Table 1 the device parameters of the best devices in iPSCs with **SAM1**, **SAM2**, **SAM3** and EADR03 as hole-selective contacts. On one hand, SAMs efficiencies are close to the efficiency of our reference devide made with EADR03, indicating that SAMs can be successfully used in iPSCs. The slight difference being 18.86 % of PCE for **SAM1** and 20.18 % of PCE for EADR03 can be attributed to the hysteresis observed in *J-V* curves. Moreover, on the other hand, the different efficiencies obtained between **SAM2** and **SAM3** were not very noticeable which means that even if they are composed by diffent functional groups, the effect in a complete device was not really distinguished in terms of efficacy.

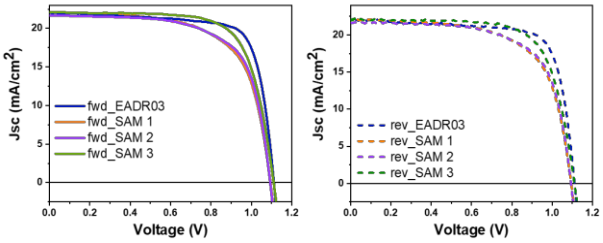

Figure 4. Device performance forward and reverse direction of the different SAMs and EADR03 as a reference.

Table 1. Photovoltaic parameters of the champion devices of the different SAMs

HTM	Scan direction	Jsc (mA/cm^2)	Voc (V)	FF (%)	Efficiency (%)
SAM 1	forward	21.7	1.11	78.3	**18.86**
	reverse	21.91	1.11	74.7	18.09
SAM 2	forward	20.32	1.09	79.3	**17.61**
	reverse	20.46	1.09	79.9	17.85
SAM 3	forward	21.03	1.13	73.8	**17.55**
	reverse	21.04	1.12	73.3	17.40
EADR03	forward	21.06	1.12	80.09	**20.18**
	reverse	21.09	1.13	80.08	20.18

7. Conclusions

In summary, we designed and synthesized three new carbazole-based molecules as a self-assembled hole-selective materials. SAM1, SAM2 and SAM3 used in iPSCs achieving PCE of 18.86 %, 17.61 % and 17.55 %, respectively. Our results demonstrate that conjugated molecules of SAM-based carbazole have great potential for further advancing iPSCs.

References

[1] F. Alta, "Best Research-Cell Efficiencies," *NREL*, 2023. https://www.nrel.gov/pv/cell-efficiency.html

[2] G. Li *et al.*, "Highly efficient p-i-n perovskite solar cells that endure temperature variations," *Science (1979)*, vol. 379, no. 6630, pp. 399–403, 2023, doi: 10.1126/science.add7331.

[3] B. Roose, Q. Wang, and A. Abate, "The Role of Charge Selective Contacts in Perovskite Solar Cell Stability," *Adv Energy Mater*, vol. 9, no. 5, pp. 1–20, 2019, doi: 10.1002/aenm.201803140.

[4] K. Choi *et al.*, "A Short Review on Interface Engineering of Perovskite Solar Cells: A Self-Assembled Monolayer and Its Roles," *Solar RRL*, vol. 4, no. 2, pp. 1–20, 2020, doi: 10.1002/solr.201900251.

[5] E. Arkan *et al.*, "Effect of functional groups of self assembled monolayer molecules on the performance of inverted perovskite solar cell," *Mater Chem Phys*, vol. 254, no. July, p. 123435, 2020, doi: 10.1016/j.matchemphys.2020.123435.

[6] E. Arkan *et al.*, "Influence of end groups variation of self assembled monolayers on performance of planar perovskite solar cells by interface regulation," *Mater Sci Semicond Process*, vol. 123, no. July 2020, 2021, doi: 10.1016/j.mssp.2020.105514.

[7] A. Magomedov *et al.*, "Self-Assembled Hole Transporting Monolayer for Highly Efficient Perovskite Solar Cells," *Adv Energy Mater*, vol. 8, no. 32, 2018, doi: 10.1002/aenm.201801892.

[8] A. Al-Ashouri *et al.*, "Conformal monolayer contacts with lossless interfaces for perovskite single junction and monolithic tandem solar cells," *Energy Environ Sci*, vol. 12, no. 11, pp. 3356–3369, 2019, doi: 10.1039/C9EE02268F.

[9] E. Yalcin *et al.*, "Semiconductor self-assembled monolayers as selective contacts for efficient PiN perovskite solar cells," *Energy Environ Sci*, vol. 12, no. 1, pp. 230–237, 2019, doi: 10.1039/c8ee01831f.

[10] Q. Jiang *et al.*, "Surface reaction for efficient and stable inverted perovskite solar cells," *Nature*, vol. 611, no. 7935, pp. 278–283, 2022, doi: 10.1038/s41586-022-05268-x.

[11] F. Ali, C. Roldán-Carmona, M. Sohail, and M. K. Nazeeruddin, "Applications of Self-Assembled

Monolayers for Perovskite Solar Cells Interface Engineering to Address Efficiency and Stability," *Adv Energy Mater*, vol. 10, no. 48, pp. 1–24, 2020, doi: 10.1002/aenm.202002989.

[12] S. Zhang *et al.*, "Conjugated Self-Assembled Monolayer as Stable Hole-Selective Contact for Inverted Perovskite Solar Cells," *ACS Mater Lett*, vol. 4, no. 10, pp. 1976–1983, 2022, doi: 10.1021/acsmaterialslett.2c00799.

[13] E. Aktas *et al.*, "Understanding the perovskite/self-assembled selective contact interface for ultra-stable and highly efficient p-i-n perovskite solar cells," *Energy Environ Sci*, vol. 14, no. 7, pp. 3976–3985, Jul. 2021, doi: 10.1039/d0ee03807e.

[14] Z. Li *et al.*, "Simple and robust phenoxazine phosphonic acid molecules as self-assembled hole selective contacts for high-performance inverted perovskite solar cells," *Nanoscale*, 2022, doi: 10.1039/d2nr05677a.

[15] W. Li, M. Cariello, M. Méndez, G. Cooke, and E. Palomares, "Self-Assembled Molecules for Hole-Selective Electrodes in Highly Stable and Efficient Inverted Perovskite Solar Cells with Ultralow Energy Loss," *ACS Appl Energy Mater*, 2022, doi: 10.1021/acsaem.2c02880.

[16] E. Aktas *et al.*, "Role of Terminal Group Position in Triphenylamine-Based Self-Assembled Hole-Selective Molecules in Perovskite Solar Cells," *ACS Appl Mater Interfaces*, vol. 14, no. 15, pp. 17461–17469, 2022, doi: 10.1021/acsami.2c01981.

[17] M. Saliba *et al.*, "Cesium-containing triple cation perovskite solar cells: Improved stability, reproducibility and high efficiency," *Energy Environ Sci*, vol. 9, no. 6, pp. 1989–1997, Jun. 2016, doi: 10.1039/c5ee03874j.

[18] L. Leonat, G. Sbârcea, and I. V. Brânzoi, "CYCLIC VOLTAMMETRY FOR ENERGY LEVELS ESTIMATION OF ORGANIC MATERIALS," *Bull., Series B*, vol. 75, no. 3, 2013.

[19] N. Elgrishi, K. J. Rountree, B. D. McCarthy, E. S. Rountree, T. T. Eisenhart, and J. L. Dempsey, "A Practical Beginner's Guide to Cyclic Voltammetry," *J Chem Educ*, vol. 95, no. 2, pp. 197–206, Feb. 2018, doi: 10.1021/acs.jchemed.7b00361.

Urinary untargeted analysis by Arrow-SPME-GC-MS

Maria Llambrich[1], Noelia Ramírez[1,2], Raquel Cumeras[1,3], Jesús Brezmes[1]

[1] Metabolomics Interdisciplinary Group MiL@b, Department of Electrical Electronic Engineering and Automation, Universitat Rovira i Virgili (URV), IISPV, CERCA, 43007 Tarragona, Spain; phone 977559700; fax 977 55 96 99; maria.llambrich@urv.cat; noelia.ramirez@urv.cat; raquel.cumeras@urv.cat; jesus.brezmes@urv.cat [2] Pediatrics, Nutrition and Human Development Research Unit, Metabolic and Nutrition Diseases Department, Institut d'Investigació Sanitària Pere Virgili (IISPV), CERCA, 43204 Reus, Spain. [3] Translational, Epidemiological and Clinical Oncological Research Group, Oncology Department, IISPV, CERCA, 43204 Reus, Spain.

Abstract

The examination of volatile organic compounds (VOCs) in human urine samples has gained significant attention in clinical research. Among the various techniques available, SPME-GC-MS has emerged as a popular choice for analysis. In this study, we present the development of Arrow SPME, which is optimized for the untargeted analysis of urine samples. The experimental findings indicated that the optimal conditions involved using 2ml of urine with 0.25% w/w of NaOH, extracted over a period of 60 minutes at a temperature of 53ºC. Moreover, the effectiveness of this method was successfully demonstrated through the analysis of real urine samples. Notably, there was a distinct variation in the volatile profiles of samples obtained from individuals with low and high exposure to tobacco.

1. Introduction

Volatile organic compounds are a group of chemicals found in various biological fluids, including human urine. These compounds are of great importance in clinical research, as they can be used as biomarkers to diagnose and monitor various diseases[1]. In addition, VOCs can provide insight into the metabolic processes occurring within the body, and can even indicate exposure to environmental toxins or pollutants[2].

However, urine as a complex matrix efficient extraction of the interest compounds. One popular technique for the extraction of VOCs in human urine samples is solid-phase microextraction (SPME) [3]. This technique involves the use of a small, stationary phase-coated fiber that is exposed to the headspace of a urine sample. The VOCs present in the headspace are adsorbed onto the fiber and can then be desorbed and analysed using gas chromatography-mass spectrometry (GC-MS) [3]. GC-MS is highly sensitive and specific and can be used to detect a wide range of VOCs in urine samples, including endogenous and exogenous compounds [4].

Here, we present an optimization of the SPME Arrow for untargeted analysis of human urine. The optimization includes a comparison with conventional SPME Arrow fibers to prove the performance. And an application to compare individuals exposed to tobacco pollutants.

2. Methodology

2.1 Reference standards

The volatile compounds were obtained from Sigma-Aldrich Co., Ltd.: 2-pentanone, 2-hexanone, 2-heptanone, 2-nonanone, toluene, dimethyl trisulfide, nonanal, decanal, indole, 1-dodecanol, tetradecanoic acid, and 4-fluorobenzaldehyde (IS). A working solution of 50 $mg \cdot L^{-1}$ was prepared in methanol.

2.2 Samples

The optimization was performed using a pooled urine from 4 healthy individuals (age 22-27years). Samples were directly aliquoted and stored ad -80ºC before analysis. We selected 20 participants living in smokers' homes from THSExposure project. Individuals were divided into low and high exposure group, considering a high exposure when one adult resident smoke at least 10 cigarettes per day. Quality control samples were prepared pooling an equal volume of urine from all subjects.

2.3 Method optimization

The following parameters were optimized: Arrow SPME fiber coating (CAR/PDMS, DVB/PDMS, PDMS, DVB/CAR/PDMS, PA), volume (1 ml, 1.5ml, 2 ml, and 3 ml), salt volume (no salt, 0.1% w/w, 0.25% w/w, saturation). A central composite design was applied for temperature, incubation time and extraction time.

2.4 Analysis

All analysis were carried out on a GC TRACE 1310 – MS Exactive (Thermo Fisher) equipped with a PAL Autosampler and a temperature-controlled drawer. We used a ZB-5plus analytical column (30m × 0.32mm × 0.25µm). Analyses were performed using SPME headspace into a splitless with helium constant flow of 1 mL·min-1. The GC oven temperature was held at 40°C for 2 min, then raised to 300°C at a rate of 10ºC/min, and held for 2 min. Fiber was desorbed at the injector port at 260ºC for 5 min. The mass spectrometer acquired m/z ratios between 35 and 400Da and an electron impact energy of 70 eV.

Identification of compounds was performed based on comparisons of mass spectra, and retention indices (RI) with NIST20 library or pure standards when available. A mixture of C7-C20 hydrocarbons was used for RI calculation. Data acquisition was performed with

Xcalibur Software (Thermo Fisher Scientific). Quant browser (ThermoFisher Scientific) was used for deconvolution, peak-picking and integration. Mass spectra were searched in NIST 20 including the corresponding RI. All statistical analysis and plots were performed with R statistics.

3. Results

The optimal extraction conditions were selected based on the performance for a mixture of 11 standards. Two approaches were used: univariate approach for coating, volume and salt addition resulting in the selection of CAR/PDMS fiber, 2mL or urine and addition of 0.25% w/w of NaOH. Then design of experiment for temperature, extraction and incubation time disclose the optimal conditions of 53ºC for 60 min extraction (See Figure 1). These conditions were used for the following experiments.

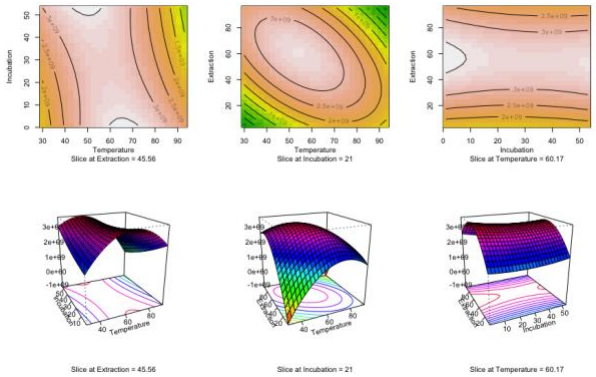

Figure 1. Central composite design curves. Representation of the interaction between temperature, incubation time and extraction time.

To assess the repeatability and reproducibility of the optimized method, we calculated the relative standard deviation (RSD) using 5 replicates of the pooled urine. We observed that samples kept at 4ºC before analysis exhibited an increase in the number of linear and reproducible peaks compared to room temperature. Furthermore, repeatability and reproducibility of the method also improved when samples were stored at 4ºC (See Figure 2).

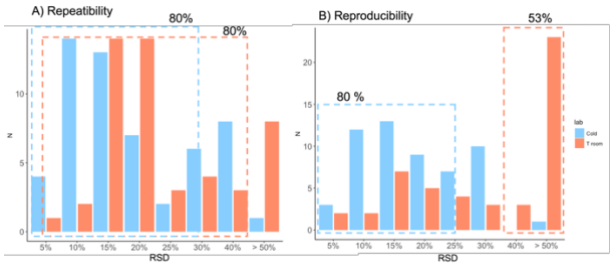

Figure 2. Method quality parameters, based on RSD. A) Repeatibility, and B) Reproducibility.

The optimized method was successfully applied to real urine samples from 20 children residing in homes where smoking occurs. A total of 131 features were detected, and after the filtering out process, we were able to identify 63 compounds. We found 6 compounds that exhibited significant differences between groups: N-acetylisopropylbarbituric acid; p-cresol; isodurene; alpha-terpineol; naphthalene, 1,2-dihydro,1,16-trimethyl; and p-cymene. Among them, p-cresol, p-cymene, isodurene and alpha-terpinol were associated with high exposure to tobacco at home.

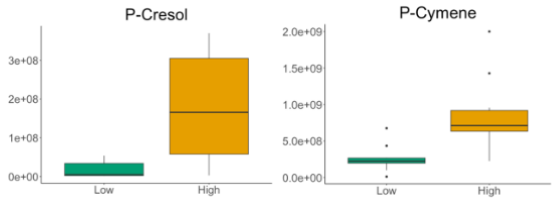

Figure 3. Boxplot comparison of P-Cresol and P-Cymene for High and Low group.

4. Conclusions

The study presented an optimized and quality-controlled method for untargeted urinary Volatilomics with Arrow SPME-GC-MS. Future applications were demonstrated by the ability to differentiate between urinary profiles of individuals with low and high exposure to tobacco.

Acknowledgments

This work has been supported by Spanish MINECO (RTI2018-098577-B-C21, PID2021-126543OB-C22). This project received funding from the European Union's Horizon 2020 research and innovation programme under the Marie Sklodowska-Curie grant agreement No (798038). MLL is thankful for her URV graduate fellowship PMF-PIPF program (2019PMF-PIPF-37). We acknowledge AGAUR consolidated group grants (2017SGR1119, 2021SGR00842). IISPV is a member of the CERCA Programme/Generalitat de Catalunya.

References

[1] B. R. B. da Costa and B. S. De Martinis, "Analysis of urinary VOCs using mass spectrometric methods to diagnose cancer: A review," Clinical Mass Spectrometry, vol. 18, pp. 27–37, 2020

[2] W. Filipiak et al., "Dependence of exhaled breath composition on exogenous factors, smoking habits and exposure to air pollutants," J Breath Res, vol. 6, no. 3, 2012

[3] S. Zhang and D. Raftery, "Headspace SPME-GC-MS Metabolomics Analysis of Urinary Volatile Organic Compounds (VOCs)," 2014, pp. 265–272.

[4] N. Drabińska et al., "A literature survey of all volatiles from healthy human breath and bodily fluids: The human volatilome," J Breath Res, vol. 15, no. 3, 2021

A photoluminescence-based sensor for the detection of Endoglin for the early diagnosis of Preeclampsia

Josep Maria Cantons, Akash Bachhuka*, Lluis F. Marsal*

Departament d'Enginyeria Electrònica, Elèctrica I Automàtica, Universitat Rovira i Virgili, Avinguda Països Catalans 26, 43007 Tarragona, Spain; Phone: 977 55 85 24
***Email: akash.bachhuka@urv.cat, lluis.marsal@urv.cat**

Abstract

Endoglin (ENG-105) is a globular glycoprotein with a high molecular weight. It is reported to be present in early stages of Preeclampsia [1]. Its concentration increases during different diseases or decreases during treatment, making it an effective therapeutic target [2] for diagnosis and prognosis. That makes endoglin an attractive candidate as a biomarker for our biosensor. This research project aims to fabricate a proof-of-concept (POC) device to detect near real-time changes in the concentration of endoglin. Nanoporous anodic alumina (NAA) will be used to fabricate the POC device. The combination of photoluminescence properties of NAA [3] and the photoluminescence of gold nanoclusters will be used in order to test different concentrations of Endoglin. The results showed a quenching in the photoluminescence (PL) as we increased the Endoglin concentration, showing a linear range from 1 ng/mL to 50 ng/mL.

1. Introduction

Preeclampsia is a common complication of pregnancy that affects 5 – 8% of pregnant women after the 20 weeks of gestation that affects a total of 8.5 million women worldwide [4]. It is defined as a hypertensive disorder [5] that has a high incidence rate of fetal, maternal, and infant mortality. Endoglin has been reported as a potential biomarker that is present in Preeclampsia disease, due to its high levels in plasma for women with this complication. The concentration of Endoglin increases to around 20 ng/mL and it starts being a problem but with a low risk for the woman. The aim of the study is to detect Endoglin for the early detection of Preeclampsia by combining the PL properties of gold nanoclusters and NAA.

2. Materials and Methods

Materials

High-purity aluminum substrates (99.999%) with a thickness 0.5 mm, Ethanol, acetone, oxalic acid, perchloric acid, chromic acid, Glutathione reduced, gold III chloride, Hydrogen peroxide, 3-Aminopropyltriethoxysilane, 1-ethyl-3-(3-dimethyl aminopropyl) carbodiimide, N-hydroxy succinimide, Glucose Oxidase. Bovine Serum Albumin and Human Serum Albumin. Recombinant human CD105 protein (ab54338) (Endoglin) and Recombinant Anti-CD105 antibody [EPR19911-220] (ab252345).

Fabrication

Nanoporous alumina samples were fabricated by anodizing aluminium using a two-step anodization method. In this whole procedure, 0.3 M oxalic acid at 5 ºC was utilized. The method consists of first anodization lasting 20 hours at 40 V, where the pores start growing. The next step is to remove all the alumina from the surface by etching with chromic acid at 70 ºC for 3 hours. This step aims to obtain the aluminium surface with tiny holes from which the pores will grow in an ordered way. Once this intermediate step is done, the samples are exposed to second anodization, which utilizes the same acid and voltage conditions as the first anodization. Additionally, sample thickness is controlled by varying the charge. In our case, we wanted 6 µm of pore length, so we applied a total of 95 C for four samples anodized simultaneously. Additionally, we employed an extra step called pore widening, using phosphoric acid 5 % at 35 ºC. In this temperature condition, the growth of the pores is expected to be 1-1.5 nm/s, so we apply a pore widening reaction for 20 minutes to obtain pores up to 65 nm.

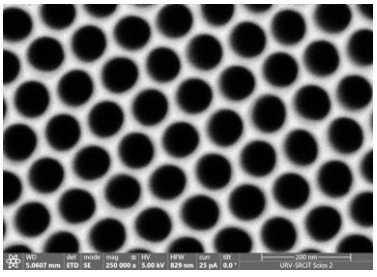

Fig.1. FESEM image of a NAA sample after the whole fabrication procedure.

APTES functionalization

The surface of the NAA was functionalized by APTES, which consists of the binding of amino groups on the alumina surface. This functionalization generates amino groups facilitating the immobilization of different biomolecules making the sensor selective. The first step in APTES functionalization is the hydroxylation of the surface. After the hydroxylation, the samples are stored for 1h at 60 ºC in the oven to ensure that the hydroxyl groups have attached to the NAA surface. Finally, the samples are exposed to 9.5 mL of toluene and 0.5 mL of 5% APTES. This last step aims to attach silane and amine groups to the hydroxylated alumina surface. Once the step is done, we keep the samples for 1h at 100 ºC to promote the silane cross-linking.

Surface activation and gold nanoclusters binding

The surface activation is done using 1-ethyl-3-(3-dimethyl aminopropyl)carbodiimide (EDC) and N-hydroxysuccinmide (NHS). The NHS/EDC solution is prepared in a 1:1 ratio of 6 mg of EDC and 10 mg of NHS and mixed with 2 nm gold nanoclusters solution (previously synthesized). The NHS/EDC reaction activates the carboxyl groups of the gold nanoclusters to bind them to amine-functionalized surfaces. We added 500 µL of the activated gold nanoclusters to the amine-functionalized NAA surface for 1 hour, followed by washing with deionized water.

Fig.2. Gold nanoclusters solution incubated on NAA samples.

After the gold binding on the APTES functionalized surface, an antibody functionalization is carried out in order to make the sensor selective to Endoglin.

3. Results

Photoluminescence spectroscopy was utilized to characterize the photoluminescence signal from the gold nanoclusters solution, nanoporous alumina, and gold nanoclusters bound to the NAA surface. The sensing experiments were carried out by analysing the changes in the PL intensity for different endoglin concentrations (1 ng/mL, 10 ng/mL. 20 ng/mL, 30 ng/mL, 50 ng/mL, 100 ng/mL and 500 ng/mL). The results showed a PL quenching as we increased the concentration of endoglin. The sensor presented a linear behaviour from the 1 ng/ml to 50 ng/mL as it is observed in Figure 3. Moreover, it presented a linearity of R2 = 0.97. The linear range shows us that the sensor can work for the early detection of Preeclampsia.

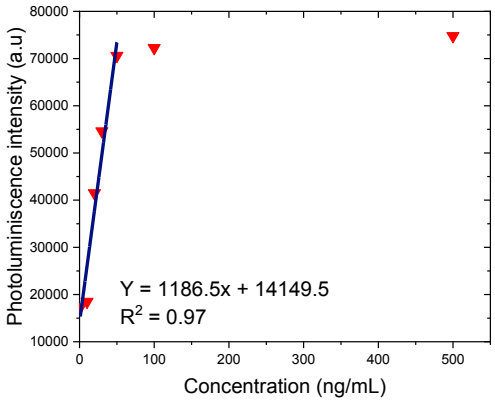

Fig.3. Response and linear behavior of the sensor from 1 – 50 ng/mL.

4. Conclusions

In this work we performed a POC device based on NAA and gold nanoclusters for the detection of ENG-105. To test the sensor, different concentrations from 1 – 500 ng/mL were used, and the results showed a quenching in the PL as we increased the ENG-105 concentration. The results also showed a linear detection range from 1 – 50 ng/mL matching with the range where Preeclampsia is present.

References

[1] Rana S, Cerdeira AS, Wenger J, Salahuddin S, Lim KH, Ralston SJ, Thadhani RI, Karumanchi SA. PLoS One. 2012;7(10).

[2] Fonsatti, E., Altomonte, M., Nicotra, M. et al. Oncogene 22, 6557–6563 (2003).

[3] I. V. Gasenkova, N. I. Mukhurov, S. P. Zhvavyi, E. E. Kolesnik, and P. Stupak, J. Lumin, vol. 185, pp. 298–305, 2017.

[4] Anderson, U. D., Olsson, M. L. V., Kristensen, K., Åkerström, B., & Hansson, S. R. (2012). Review: Biochemical markers to predict preeclampsia. Placenta, 33, S42–S47.

[5]. Buurma, A., Turner, R. J., Driessen, J. H. M., Mooyaart, A. L., Schoones, J. W., Bruijn, J. A., Bloemenkamp, K. W., Dekkers, O. M., & Baelde, H. J. (2013). Genetic variants in pre-eclampsia: a meta-analysis. Human Reproduction Update, 19(3), 289–303

Electropulsed Nickel Nanorods deposition using Nanoporous Anodic Alumina as templates for Energy Storage Applications

Tabish Aftab, Josep Ferré i Borrull, Lluis F. Marsal*
Eng. Electrònica, Elèctrica i Automàtica, Universitat Rovira i Virgili, Paisos Catalans-26, Tarragona–43007, Spain
tabish.aftab@urv.cat, josep.ferre@urv.cat, *lluis.marsal@urv.cat

Abstract

This work presents the fabrication of Nickel nanorods by electropulsed deposition method using nanoporous anodic aluminum oxide (AAO) templates and demonstrates the electrochemical properties generated by the nanostructured free-standing nickel nanorods electrodes. AAO membranes were prepared by electrochemical anodization of Al in 0.3 M oxalic acid electrolyte. Electropulsed nickel deposition on AAO was performed by controlled AC current using commercially available Watts Bath solution. Scanning electron microscopy (SEM) images confirm that the nickel nanorods formed onto AAO pores have characteristic free-standing nanorod morphology as a result of the ion-reduction process into the pores of alumina during nickel deposition. The electrochemical properties of nickel deposited AAO will be tested by measuring cyclic voltammetry (CV), galvanostatic charge–discharge and impedance spectroscopy measurements.

1. Introduction

Energy storage materials such as batteries and supercapacitors (SC's) are currently being heavily investigated as primary energy sources for vehicles and portable electronic devices. These applications require high energy and high-power energy storage devices with small masses and small volumes. Therefore, it is important that the materials for these devices will have both high gravimetric and high volumetric energy and power densities [1]. Generally, nanosizing these energy storage materials has proven to be a great method to create these high energy and power densities; however, these metrics are regularly normalized to only the electroactive material. SCs store charge electrostatically on the surface of these active material rather than as a chemical state. Based on a charge storage mechanism, SCs can be charged quickly for millions of charge-discharge cycles, leading to high power density. The problem with SCs is their low energy density, i.e., energy stored per unit active material weight is very small. Therefore, we proposed here the nanostructured metallic material (Nickel) which provides high conductivity and more surface area for charge to store. Porous anodic alumina was used as template to deposit nickel inside the pores by electropulsed deposition methodology [2-3] and later remove the alumina pores to obtain free standing nickel nanorods which were investigated extensively as electrode material for supercapacitor.

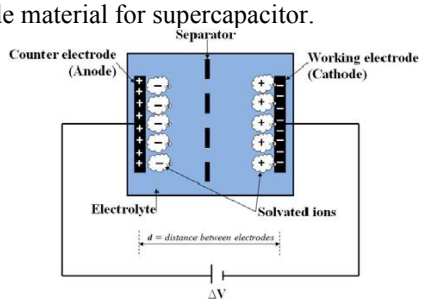

Fig 1: Schematic diagram of double layer electrochemical supercapacitor

2. Experimental Description

AAO substrates were fabricated by 2-step electro-chemical anodization using 99.99% pure aluminum sheet. Aluminum sheets with thicknesses of 0.5 mm were cut with the size of 2 × 2. For pretreatment, electropolishing was applied at 5°C under 20 V for 4 min in a 1:4 mixture of perchloric acid and ethanol through continuous stirring to remove the natural oxide layer from the surface. After the electro-polishing, first step anodization was performed on the Al surface by using an 0.3 M oxalic acid solution at 5°C at 40 V for 20h. In order to get the self-ordered pores, the alumina layer was etched chemically in 1 M phosphoric acid for 90 min at 70°C.

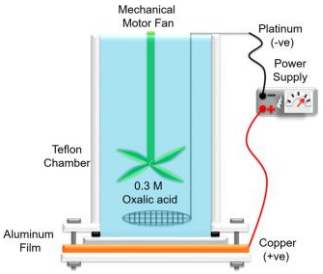

Fig 2: Schematic illustration of the fabrication process of porous alumina by electrochemical anodization.

The second anodization, which controls the depth of pores, was performed upto 72 C charge deposition for a depth of 5 µm. The diameter of the pores, Dpo= 25-35 nm, is usually formed by 0.3 M oxalic acid solution. The pore diameter was determined using SEM.

For the deposition of metallic nickel, we need to have the metallic contact between pores and aluminium substrate which was hindered by the barrier layer. To remove this barrier layer we again performed third anodization which started from the same current level as the second but this time we reduced the current step-wise with a constant factor (0.71) which reduces the potential across the samples resulting into the thinning of the barrier layer. After the third anodization, still there remains a thin barrier layer which later removed by final etching step where the sample was immersed in 5 wt% phosphoric acid at 35 ℃ for 15 minutes to remove the residual barrier layer completely. This final etching step provides metallic contact between pores and aluminum which is necessary for the homogeneity of the nickel during electropulsed deposition over the surface of the sample.

Electropulsed deposition is a current controlled method unlike dc electrodeposition which is voltage controlled. Nickel electropulsed deposition was performed using the solution of Nickel sulphate hexahydrate and Nickel chloride hexahydrate along with boric acid as buffer, commonly known as Watts Bath. In this method current is applied in the form of constant current pulses which allows the reduction of Ni-ions and their deposition at the bottom of the pores The Voltage follows the current pattern and the potential across the alumina within the cell changes correspondingly according to the applied current needed for deposition.

3. Result and Discussion

The SEM image of AAO layer is shown in Fig. 3(a) and (b). The pore diameter of AAO was measured from the SEM image as 25-35 nm. After electropulsed deposition of nickel for the required charge of 3 coulomb, free-standing nickel nanorods were observed on the AAO as shown in figure 3(d).

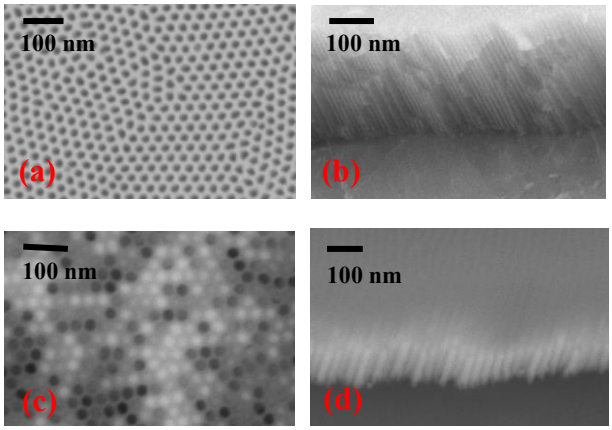

Fig. 3: SEM images, Nanoporous anodic alumina AAO (a) top view and, (b) cross sectional view.
Electropulsed deposition of Ni onto nanoporous anodic alumina, (c) top view and (d) cross sectional view

Nickel deposition into the nanopores was also confirmed by UV-vis reflactance spectroscopy. The reflectance spectra of Ni@AAO is low as compared to the reference AAO spectra which confirms the absorption of uv-light by the metallic nickel deposited in the pores.

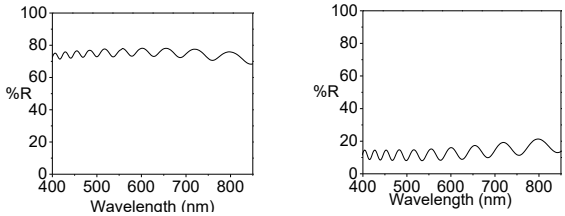

Fig. 4: UV-Vis. Spectra of (a) Nanoporous anodic alumina AAO substrate without barrier layer, and (b) Ni electropulsed deposited AAO substrate

These obtained Ni@Al substrates can be used as a nanostructured electrode for a supercapacitor. Two such films bonded back-to-back make a single supercapacitor device. The Ni nanorods segment of each electrode remains in contact with the Al layer could act as the current collector. The electrochemical properties and capacitive behaviour of the supercapacitor electrodes will be studied by cyclic voltammetry (CV), galvanostatic charge–discharge and impedance spectroscopy measurements. In order to compare the supercapacitor performance of our Ni@AAO hybrid electrodes with simple two Al-electrode supercapacitor, electrochemical measurements were also carried out for the supercapacitor devices with AAO template-grown electrodes where a thermal evaporated metal layer acted as the current collector.

4. Conclusions

In this work we have discussed the fabrication of nano porous anodic alumina by 2-step process using oxalic acid as electrolyte. Using electropulsed deposition, nickel was deposited into the pores of alumina. It has also been proposed that this free-standing Ni nanorods can be used as an electrode for supercapacitor. The electrochemical properties will be tested by cyclic voltammetry (CV), galvanostatic charge–discharge and impedance spectroscopy measurements to measure the performance of the supercapacitor.

References

[1] Liang Kun, Lei Li, and Yang Yang. "Inorganic porous films for renewable energy storage." ACS Energy Letters 2, no. 2 (2017): 373-390.

[2] Nielsch, Kornelius, Frank Müller, AP. Li, and Ulrich Gösele. "Uniform nickel deposition into ordered alumina pores by pulsed electrodeposition." Advanced Materials 12, no. 8 (2000): 582-586.

[3] Santos Abel, Lukas Vojkuvka, María Alba, Victor Balderrama, Josep Ferré-Borrull, Josep Pallares, and Lluís F. Marsal. "Understanding and morphology control of pore modulations in nanoporous anodic alumina by discontinuous anodization." physica status solidi (a) 209, no. 10 (2012): 2045-2048.

Advanced nanostructures for SERS measurements

Gohar Ijaz Dar, Elisabet Xifre-Perez, Lluís F. Marsal*
Nanoelectronic and Photonic Systems, Department of Electronics, Electric, and Automatic Control Engineering, Rovira i Virgili University, Avda. Països Catalans 26, 43007 Tarragona, Spain
E-mail: lluis.marsal@urv.cat
E-mail: goharijaz.dar@urv.cat

Abstract

Surface-enhanced Raman spectroscopy (SERS) with enormous enhancements has shown great potential in ultrasensitive detection technologies, but the fabrication of large-scale, controllable, and reproducible substrates with high SERS activity is a major challenge. From its early 1974 description, surface-enhanced Raman scattering (SERS) has attracted considerable attention due to its potential utility in a wide variety of fields throughout the life sciences, including analytical chemistry, biomedicine, agriculture, and more. To create SERS-based ultrasensitive sensors of diverse substances, highly branched metal nanostructures are of great interest. Here, we report the preparation of Au nanoparticle arrays for SERS-active substrates with tuneable particle sizes and interparticle gaps, and the enhancement factor of the SERS signals. As the fabrication protocol of such a SERS substrate is simple and inexpensive, this substrate may anticipate a wide range of applications in SERS-based sensors [1].

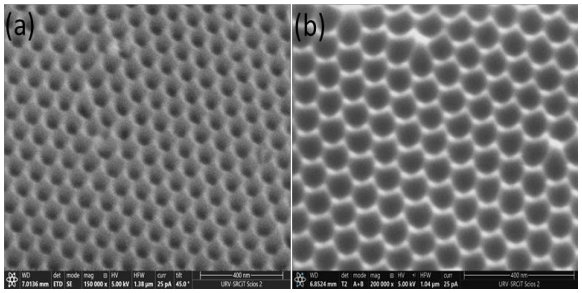

Fig 1. The Al templates shown the (a) tilted view of the porous anodic alumina and (b) showed tilted view of the Al nanoconcavities.

The Nano porous AAO was created by a two-step anodization method that used 0.3 M oxalic acid as the electrolyte at 15 °C and 40 V, as was detailed in the preceding section. The initial step consisted of an anodization that lasted for 18 hours, which was then followed by the chemical etching of the pores that were generated by treatment in an aqueous combination of chromic acid (1.8 weight%) and phosphoric acid (6 weight%) for 2 hours at a temperature of 70 degrees Celsius. To obtain nanopores, the second anodization was carried out for a period of two hours. After that, to create the concave-like shapes, Al samples were etched at a temperature of 70 degrees Celsius for one hour using an etching solution. During the initial phase of the anodization process, we used both the hard and mild anodization processes on samples that had been created using phosphoric acid. In the first phase, a voltage of 175 V was applied for an initial period of 3 hours. After that, the voltage was increased at a rate of 0.01 V/sec until it reached 195 V and remained there for 18 hours. Keep in mind that because of the high voltage, the temperature should be as low as -11 degrees Celsius while you are dealing with phosphoric acid. To obtain the nanopores, the second stage consisted of continuing to work under the same circumstances for a period of two hours [2].

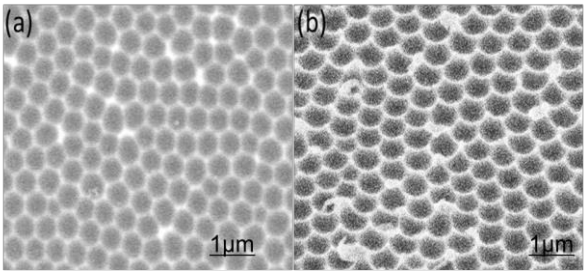

Fig.2 The FESEM images shown of the prepared Al template The FESEM images shown of the prepared Al template with (a) Au sputtering of 25 sec. Al sheet annealing for 300 °C for 30 min (b)The tilted image of the Al template.

The gold layer starts to interact with the topography of the intentionally manufactured nano concavities when the gold-coated nanoarrays are subjected to heat annealing [3]. This is because the nano concavities were formed artificially. Obtaining varying distributions and/or sizes of AuNPs required using a variety of sputtering periods and annealing temperatures for the Au film. The formation of gold nanoparticles (Au NPs) onto dense nanoarrays created by electrochemistry results in a honeycomb-like structure with high spatial resolution. They are efficient substrates for sensitive applications, notably for SERS, displaying strong Enhancement Factors for the detection of molecules, and their plasmonic features have been experimentally measured over a broad range, stretching from the visible to the NIR area . The findings of this study will make it possible to rapidly identify and categorize target analytes for clinical usage, food safety, environmental contamination, chemical hazards, and direct label-free detection of a variety of biological systems, such as

DNA, proteins, viruses, cells, and so on. This will be possible in several different contexts, including clinical applications, food safety, environmental contamination, chemical hazards, and food safety [4].

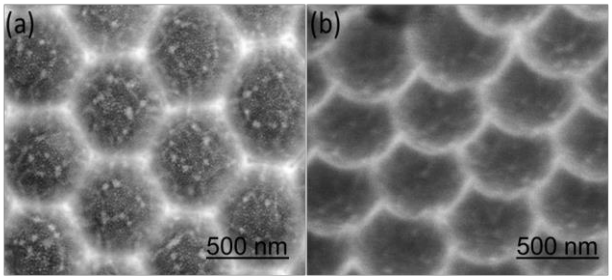

Fig.3 The FESEM images shown of the prepared Al template The FESEM images shown of the prepared Al template with (a) Au sputtering of 50 sec. Al sheet annealing for 300 °C for 30 min (b)The tilted image of the Al template.

Conclusion

In summary, the FESEM analysis showed that the different sputtering conditions and annealing conditions were leads to fascinating structures as SERS substrates for rapid detection of various probe molecules. The combination of these characteristics makes the Al template a highly attractive material for the development of a broad range of sensing devices for many applications. We expect that further progress on structural and chemical modifications of AAO will facilitate the development of AAO-based devices with superior performances. a novel fast SERS strategy will be successfully developed. The assay proved simple, cost-effective, sensitive, and selective for in situ, rapid detection.

References

[1] Choudhari, K. S., et al. "Facile fabrication of superhydrophobic gold loaded nanoporous anodic alumina as surface-enhanced Raman spectroscopy substrates." *Journal of Optics* 24.4 (2022): 044002.

[2] Dong, Jun, et al. "Nanoscale engineering of ring-mounted nanostructure around AAO nanopores for highly sensitive and reliable SERS substrates." *Nanotechnology* 33.13 (2022): 135501.

[3] Marsal, L. F., et al. "Fabrication and optical characterization of nanoporous alumina films annealed at different temperatures." Optical Materials 31.6 (2009): 860-864.

[4] Toccafondi, Chiara, et al. "Thin nanoporous alumina-based SERS platform for single cell sensing." *Applied Surface Science* 351 (2015): 738-745.

Synthesis of 2D Layered InSe Crystal by Liquid Phase Exfoliation (LPE) for Gas Sensing Application

Jyayasi Sharma, Dalal Fadil, Eduard Llobet Valero

MINOS, DEEEA, Universitat Rovira i Virgili, Països Catalans 26, 43007 Tarragona, Spain
jyayasi.sharma @urv.cat, dalal.fadil@urv.cat, eduard.llobet@urv.cat

Abstract

Transition Metal Monochalcogens (TMM´s) have emerged as a crucial technological component in the field of gas sensors because of their low cost, high sensitivity, fast response and their relative simplicity. Indium Selenide (InSe), is a material that is presently attractive due to its distinct layered morphology and electronic and optoelectronic properties that make it appropriate for photovoltaic sensing, biosensing imaging, and as a catalyst in hydrogen evolution reactions in addition to gas sensing. In this research, we created a technique for exfoliating InSe using a liquid phase exfoliation process at a minimal temperature of 30°C, with modulation in flake's lateral dimension and thickness. The flakes' structure was analysed, and its gas-sensing capabilities will be investigated.

Keywords: Liquid Phase exfoliation, gas sensing,flakes modulation

1. Introduction

Many 2D materials, including graphene and TMDs, are being investigated for their distinctive electrical and structural features for their use in sensing applications. One material whose characteristics have advanced is indium selenide (InSe), which has an extremely low intralayer Young's modulus but a high interlayer cleavage and slippage energy [1]. With an adjustable bandgap of 1.4–2.6 eV, this offers an additional benefit and is better suited for sensing films [2]. Thin films can be produced using a variety of techniques, including CVD, mechanical exfoliation, and LPE [3]. However, LPE gives an improvement in the flakes' dimension and size tunability. The quality of the nanosheets that are obtained from the LPE process is significantly influenced by a number of variables, including the solvent utilized, the ultrasonication power, the ultrasonication temperature, the processing duration, and the solute content. These elements have a direct impact on the lateral size and thickness of the nanosheets. N-Methyl-2-pyrrolidone (NMP) [4], Acetone, Dimethyl formamide (DMF), and N-Cyclohexyl-2-pyrrolidone (CHP) are the conventional solvents utilized for LPE in these materials. However, all of these solvents are artificial and pose long-term, gradual health risks. A good solvent should have a low boiling point, a good surface energy, and be environmentally benign. We have presented the LPE technique of InSe with customizable dimensions in our work with more sustainable solvent.

2. Methodology

We have created an environmentally friendly solution of InSe with IPA for the exfoliation of InSe. IPA has the benefit of a low boiling point and is less toxic than common commercial solvents like NMP, DMF, etc. The following ingredients were combined to create this solution: 10 mg of InSe, 3 mL of IPA, and 7 mL of water. Following the exfoliation, centrifugation was performed for 30 mins @ 1500 rpm, for separation of flakes based on their size and thickness. Finally, the centrifugated solution was divided into 4 parts, based on supernatant, suspended and precipitate [5]. Figure 1. depicts the whole procedure.

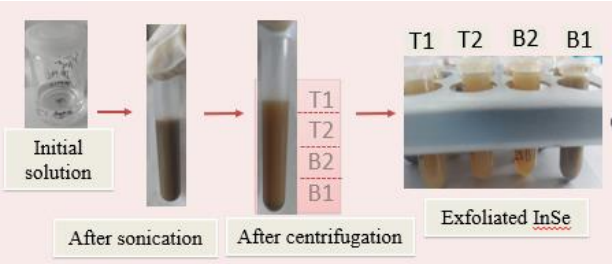

Figure 1. Liquid Phase Exfoliation of InSe.

3. Results and Discussions

To exfoliate, we used commercial InSe powder. We used FESEM to examine the structure of this powder. The stacking, stratification, and well-defined structure composed by Van Der Walls forces of InSe powder are clearly visible in the FESEM image (figure 2.). The powder was then exfoliated, and both the powder and the exfoliated flakes were subjected to EDS after being put on an alumina substrate. We discovered that the bulk powder's chemical composition and the exfoliated InSe that was deposited on the alumina substrate are both listed (figure 3.). It attests to In and Se's coexistence with quasi-free impurity. The material's deposition on the Alumina substrate is confirmed by the Al peak. Moving on, we compared the two concentrations of the solution T1 and B1 based on supernatant and precipitate of the

solution (figure 4.), and we analysed the dimensions of these flakes by particle size distribution using dynamic light scattering technique. The largest particle size that we could determine was 1406 nm for T1 and 1635 nm for B1. This clearly shows that the B1 exfoliated InSe has a larger lateral size than the T1 exfoliated InSe, which is helpful for covering the sensing layer (figure 4.)

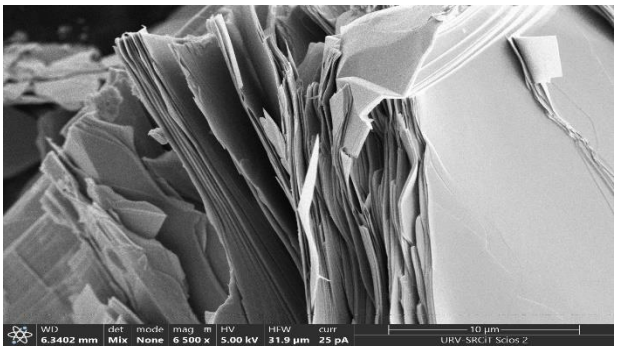

Figure 2. FESEM of InSe Commercial Powder

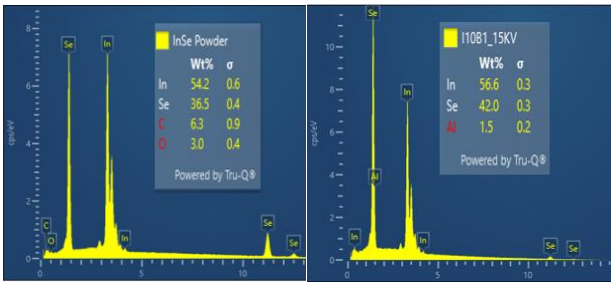

(a.) (b.)

Figure 3. EDS analysis of (a.) InSe Powder (b.) InSe exfoliated flakes deposited on Al.

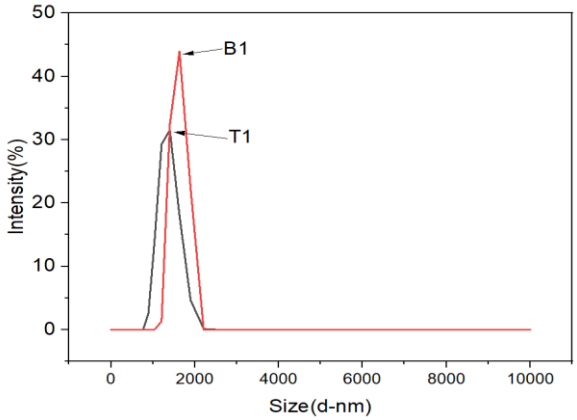

Figure 4. Particle size distribution of T1 and B1 composition in DLS.

The successful exfoliation of InSe is clearly visible in FESEM images, and this approach allows for modulating lateral dimensions and thickness. We have shown the FESEM structural study of the exfoliated flakes from the T1, T2, B2, and B1 concentrations in (figure 5). As the flakes moved from the supernatant regions T1 and T2 to the segregation regions B2 and B1, their lateral diameters considerably increased from 48 nm to 900 nm. In (figure 6) the optical absorption spectra were recorded for exfoliated InSe in range of 190 nm – 1100 nm. It shows an increase of the absorption in UV region.

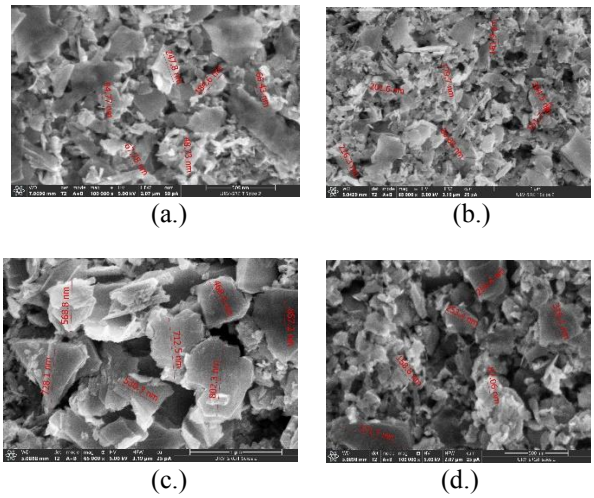

(a.) (b.)

(c.) (d.)

Figure 5. Lateral size modulation study from (a.) T1 (b.) T2 (c.) B2 (d.) B1 respectively.

Last but not least, we performed TEM on the flakes and discovered that the exfoliated nanoflakes from the T1 region are notably thinner layered than the B1 nanoflakes, which are noticeably more multi-layered as shown in (figure 6.).

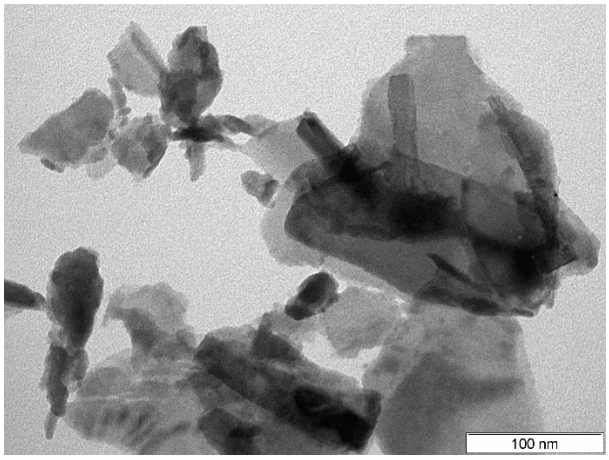

(a.)

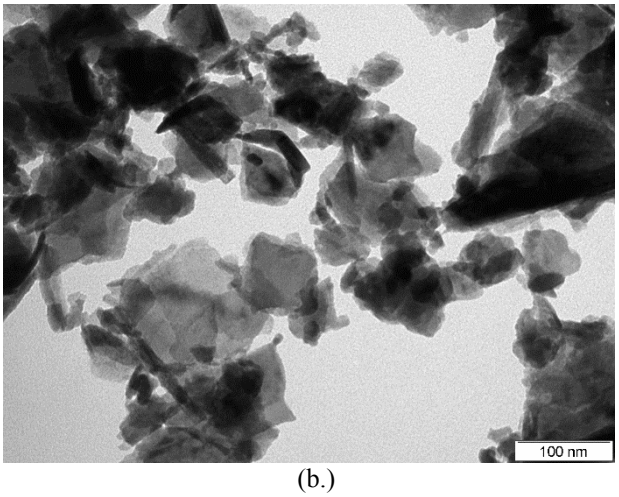

(b.)

Figure 6. TEM imaging from (a.) T1 (b.) B1 respectively, comparing thickness of the flakes.

3. Conclusions

With the Liquid Phase Exfoliation method, InSe bulk crystals were successfully exfoliated using low ultrasonication power. We prepared four sections of InSe nanoflakes. The morphology of these flakes was examined by FESEM and TEM characterisations and demonstrated the variation in thickness going from the top to the bottom of the dispersion. In addition, the particle size distribution showed decreasing of the lateral size and compromise between size and thickness during exfoliation. The optical absorption of the fourth dispersions reveals high absorbance of InSe nanoflakes in UV region. In the future, these dispersions will be tested and functionalised for optoelectronic gas sensors.

Acknowlegdements

This work has been funded by FI-SDUR grant and the European Union's Horizon 2020 research and innovation programme under the Marie Sklodowska-Curie grant agreement No. 101025770.

References

1. H. Li, et al. "Liquid phase exfoliation of indium selenide: Achieving the optimum exfoliating parameters and unraveling the mechanism" Progress in Natural Science: Materials International 2022.
2. Y. Sui, et al. "InSe: a two-dimensional material with strong interlayer coupling." Nanoscale, 2018.
3. N. Curreli, et al. "Liquid Phase Exfoliated Indium Selenide Based Highly Sensitive Photodetectors. " Advanced Functional Materials.
4. Elisa Petroni, et al."Liquid-Phase Exfoliated Indium–Selenide Flakes and Their Application in Hydrogen Evolution Reaction" Nano Micro Small Journal
5. D. Fadil et al. " On the chemically-assisted excitonic enhancement in environmentally-friendly solution dispersions of two-dimensional MoS_2 and WS_2." Journal of Materials Chemistry C, 2017

Enhancing laser-induced graphene production and tailoring for exploring their potential as wearable gas sensors

José Carlos Santos-Ceballos[1], Foad Salehnia[1], Alfonso Romero[1], Xavier Vilanova[1]

1 Universitat Rovira i Virgili, Microsystems Nanotechnologies for Chemical Analysis (MINOS), Tarragona, Spain

Abstract

The successful implementation of graphene-based sensors and electronic devices is still a difficult task, partially due to the challenges associated with integrating the production of high-quality graphene materials with existing fabrication and manufacturing processes. Therefore, it is essential to develop scalable techniques for the in-situ fabrication of graphene-like materials with desirable properties. One promising approach involves utilizing a low-cost CO_2 laser to convert polyimide into graphene. However, the optimization of this graphitization process is hindered by the complex interactions between key parameters and non-linear parameter terms. This presents a significant challenge for achieving rapid and efficient optimization using available resources. Precisely controlling the physical, chemical, and electronic properties of laser-induced graphene (LIG) is a critical factor in fabricating flexible electronic devices. However, optimizing the production of LIG is often a time-consuming and expensive process. In this project, we demonstrate the use of advanced automated parameter tuning techniques through laser stimulation combined with machine learning methods to enable rapid single-step laser patterning and structuring capabilities.

This approach aims to prepare a simulation that can be used for all CO_2 Lasers to calculate optical energy flux and combined with a machine learning technique to fabricate high-quality graphene-based gas sensors, which require precise and controlled properties of the graphene material. Applying these automated techniques can significantly reduce the time and cost associated with LIG production optimization, making it a promising strategy for the efficient and scalable manufacturing of graphene-based electronic devices.

1. Introduction

LIG is a newly emerging 3D porous material produced when irradiating a laser beam on certain carbon materials. LIG exhibits high porosity, excellent electrical conductivity, and good mechanical flexibility [1]. It has been used in sensor applications due to its unique properties such as three-dimensional microporous structure, good conductivity, and superior facile laser fabrication process [2]. LIG fibers have also been found to contain few-layer graphene with high electrical conductivity, high thermal stability, high thermal conductivity, and outstanding electrochemical performance [3]. Also, it has been used in gas sensing applications due to its high sensitivity and selectivity [4].

Laser graphitization, thus, represents an exciting technology for the direct integration of porous 3D graphene electrodes on polymer substrates. To achieve these conversions, multiple-laser passes at reduced fluences, including the use of defocused lasers to enhance laser-path overlap, are used to produce suitable quality LIG. For each feedstock material, optimization of the laser graphitization process involves identifying a suitable set (or range) of process parameters, including (average) laser power and scan speed, that will yield direct-write formation of 3D porous, graphene-like carbon. Non-optimal laser parameters can lead to unwanted side effects from over- or under-exposure. Over-exposure effects include material ablation, redeposition, oxidation, or combinations of these. Under-exposure effects include melting or incomplete graphitization. This complex materials challenge mandates optimization strategies that are both rigorous and efficient.

To carry out a correct optimization, the first step would be to create a data set, where the different combinations of the laser parameters are covered. Therefore, it would be necessary to prepare many samples, representing a significant expense of time and materials. Considering this issue, to form this data set, we have carried out a computational simulation of laser behavior. This allows us, in a very short time to have a large amount of data for optimization, which can be easily configured according to the specifications of the laser.

Our goal is to optimize sensing performance while changing the scan speed, frequency, and duty cycle of the laser hence fabrication throughput using simulation combined with machine learning methods. This provides a procedure for synthesizing LIG on a flexible substrate.

Finally, as proof of concept, we checked the optimized LIG to prepare a gas sensor to detect NO_2. The sensor design achieved to desired characteristics (geometry, conductivity) by optimization of various parameters (laser power, scan speed, frequency, and pattern design).

2. Materials, methods and results

LIG was synthesized using a two-step process on a polyimide substrate. Initially, a commercially available

polyimide film was cleaned with acetone. Subsequently, a CO_2 laser system (SYNRARD 48-2) operating at a wavelength of 10.6 µm and a power of 25 W was employed to pattern the polyimide film. The laser was focused onto the polyimide surface using a lens with a focal length of 74 mm, and the laser beam was scanned over the surface on a range of speed of 1 to 3000 mm/s and frequency in a range of 1 to 20 kHz. The laser parameters, including power duty cycle, scanning speed, and frequency, were optimized by a simulation code provided in MATLAB to calculate optical energy flux and predict LIG quality to achieve a uniform and high-quality LIG. Fig.1.b shows the simulation output (the diagram of power distribution in line) and real laser output (the laser spots on the polyimide sheet).

To manufacture the NO_2 sensor as a proof of concept, the electrode has been designed with a sensitive area of 3x6 mm^2 on the flexible substrate (Fig.1.a). The parameters of the laser were obtained from the simulation (200 mm/s, 12 kHz, 12%) to synthesize the graphene that allows the detection of the gas.

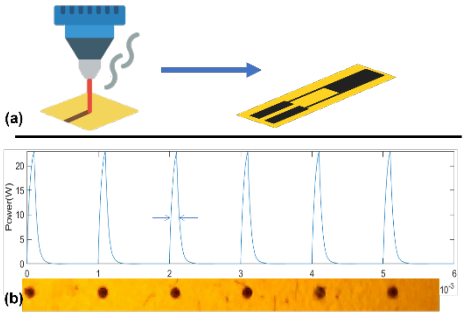

Fig.1 . Schematic illustration showing the (a) fabrication process of the LIG gas sensor and (b) comparison between simulation and real output laser.

The gas-sensing performance of LIGs was evaluated in an airtight Teflon chamber with a volume of 35 cm^3 at room temperature. The sensing chamber was connected to a gas mixing and delivery system that used calibrated gas cylinders and pure dry air as carriers. Then, the resistance of the different sensors was monitored using a multimeter (HP 34972A, Agilent), and resistance changes were recorded while different concentrations of gas were applied. To work under more realistic experimental conditions, the total flow was adjusted at a low rate (100 mL/minute) using a set of mass-flow controllers (Bronkhorst High-Tech B.V.) and electro valves. The sensors were stabilized under dry air for 120 minutes before exposure to a given concentrations of gaseous species for 60 minutes. The responses to several concentrations were recorded by applying successive dilutions of gases and defining sensor response as $\Delta R/R_0$ expressed in percentage, where ΔR corresponds to the resistance changes recorded over 60 minutes of gas exposure, while R_0 is given by the resistance of the sensor in the air (or baseline). Fig.2 shows the response of the LIG gas sensor in the presence of 10, 50 and 100 ppm of NO_2.

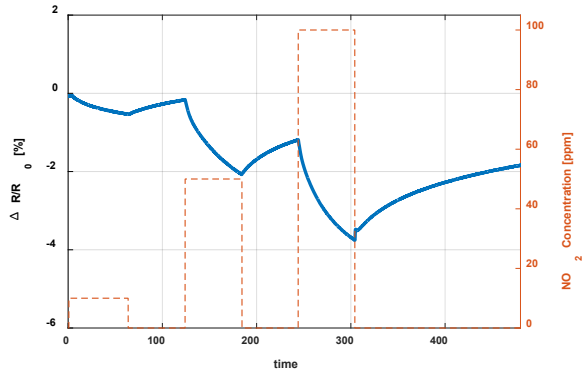

Fig.2 The gas-sensing performance of LIG gas sensor to NO_2.

3. Conclusions

The primary objective of this research project is to develop a technique for synthesizing LIG on a flexible substrate, which can be utilized for wearable gas sensing applications. By utilizing laser graphitization, this cutting-edge technology enables the direct integration of porous 3D graphene electrodes onto polymer substrates, which can be utilized for a wide range of applications. To achieve this goal, we have conducted extensive research to identify the most suitable process parameters for laser graphitization. We have optimized the process parameters, such as the average laser power, frequency, and scan speed to achieve the direct-write formation of 3D porous, graphene-like carbon. By doing so, we ensure that the resulting LIG electrodes are of the desired quality, geometry, conductivity, and thickness.

To address the complexity of this challenge, we have implemented rigorous and efficient optimization strategies. We have utilized simulation combined with machine learning methods. We have checked the optimized LIG for NO_2 gas sensing. In the next step, we plan to utilize modification approaches, such as in situ synthesis and electrochemical synthesis to prepare LIG composite for different sensing applications.

Overall, our research has made significant progress in developing a method for synthesizing LIG on a flexible substrate.

References

[1] T. S. D. Le et al., "Recent Advances in Laser-Induced Graphene: Mechanism, Fabrication, Properties, and Applications in Flexible Electronics," Advanced Functional Materials, vol. 32, no. 48. 2022.

[2] Z. Wan, N. T. Nguyen, Y. Gao, and Q. Li, "Laser induced graphene for biosensors," Sustainable Materials and Technologies, vol. 25, p. e00205, Sep. 2020.

[3] L. X. Duy, Z. Peng, Y. Li, J. Zhang, Y. Ji, and J. M. Tour, "Laser-induced graphene fibers," Carbon N Y, vol. 126, pp. 472–479, Jan. 2018.

[4] M. G. Stanford, K. Yang, Y. Chyan, C. Kittrell, and J. M. Tour, "Laser-Induced Graphene for Flexible and Embeddable Gas Sensors," ACS Nano, vol. 13, no. 3, pp. 3474–3482, Mar. 2019.

ZnO loaded graphene for NO_2 gas sensing

M.A. Alouani[1], J. Casanova-Chafer[1], F. Güell[1, 3], E. Peña-Martín[2], S. Ruiz Martínez-Alcocer[2], S. de Bernardi-Martín[2], A. García-Gómez[2], X. Vilanova[1] * and E. Llobet[1]

Universitat Rovira I Virgili
mohamedayoub.alouani@urv.cat, juan.casanova@urv.cat, xavier.vilanova@urv.cat

Abstract

This paper investigates the effect of decorating graphene with zinc oxide (ZnO) nanoparticles (NPs) for the detection of NO_2. In this regard two graphene sensors with different ZnO loadings of 5 wt.% and 20 wt.% were prepared and their responses towards NO_2 at room temperature and different conditions were compared. The experimental results demonstrate that the graphene loaded with 5 wt.% ZnO NPs (G95/5) shows better performance at detecting low concentrations of the target gas than the one loaded with 20 w.t% ZnO NPs (G80/20). Moreover, measurements under dry and humid conditions of the G95/5 sensor revealed that the material is very sensitive to ambient moisture showing an increase in NO_2 sensitivity of almost 8-fold when the background changes from dry to 70% relative humidity. Regarding sensor selectivity it presents a significant selectivity towards NO_2 compared to other gas compounds

1. Introduction

Gas sensors play an increasingly important role in our modern society, particularly for industrial gas emisión control and public health security. Among many different gases, the rapid detection of dangerous gases such as nitrogen dioxide is technologically essential as these gases are causing atmospheric contamination (green house effect) and can be dangerous for human health very above low levels of exposure. Chemioresistive sensors have been presented as one of the promising sensors for detecting these type of gases due to their high sensitivity, low cost, reproducibility and simplicity. Thanks to its extraordinary high Carrier density and mobility, Graphene was seen as the ideal candidate to make these chemioresistive gas sensors and to enhance even more these characteristics, zinc oxide nanopartices were loaded in the Graphene since ZnO is a semiconductor with a band gap of 3.37 eV and exciton binding energy of 60 meV, which makes it very useful for making stable devices. It is also considered thermally and chemically stable which makes it also perfect for the production of devices for a long period of use. But most importantly, the fact that ZnO has a good response towards different toxic gases and low cost, made it widely studied in gas sensing applications.

2. Materials and Methods

2.1. Nanocomposite synthesis and deposition

G80/20 and G95/5 nanomaterials with a weight ratio of 80:20 and 95:5, were synthesized by the insertion of zinc oxide nanoparticles in the pristine graphene nanoplatelets using a novel nanotechnological process based on patented procedures (Patent number ES2678419A1). Briefly, pristine graphene nanoplatelets were dispersed in organic acid in which the starting ZnO had been previously dissolved. After homogenization, ZnO nanoparticles were precipitated between graphene nanoplatelets with a basic solution and under controlled parameters such as agitation, temperature, or nanomaterial proportion, which can influence the crystallization process.

2.2. Sensor Fabrication

The different nanomaterials were deposited on commercial alumina (Al_2O_3) substrates via the spray coating method while heating the substrate to 70 °C.

2.4. Material characterization

The two obtained sensors were characterized using different techniques such as Raman via a Raman spectrometer (Renishaw, plc. UK) with a laser wavelength of 514 nm to check the crystallinity of the materials, Field Emission Scanning Electron Microscope (FESEM) using a Carl Zeiss AG-Ultra 55 (Germany) to study the surface morphology and to check the distribution of the NPs on the graphene layer and Photoluminiscece (PL) measurements to analyse the defects in the sensing layer. These later measurements were performed at room temperature using a chopped

Kimmon IK Series He-Cd laser (325 nm and 40 mW). Fluorescence was dispersed with an Oriel Corner Stone 1/8 74000 monochromator, detected using a Hamamatsu H8259-02 with a socket assembly E717-500 photomultiplier, and amplified through a Stanford Research Systems SR830 DSP. A filter in 360 nm was used to stray light.

2.5. Gas Sensing Measurements

The resistance changes under NO_2 gas and experimental conditions were monitored using an Agilent HP 34972A multimeter connected to the gas sensing chamber.

3. Results

3.1 Material characterization

Figure 1a shows the Raman spectra of the G95/5 sensor. Only graphene specific peaks were noticed at shifts of 1347 cm^{-1} for the D-band, 1576 cm^{-1} for the G-Band, and the 2D band at 2696 cm^{-1}. Despite the presence of the ZnO in the graphene, the peak corresponding to the NPs is absent in the spectrum due to its low concentration of 5%. The same graphene peaks were observed also in figure 1b for the G80/20 sensor with the D-band, G-band, and 2D band shifts at respectively 1351 cm^{-1}, 1579 cm^{-1}, and 2704 cm^{-1}, although in this spectrum a new peak is present at 415 cm^{-1}, which can be attributed to the ZnO nanoparticles since its specific peak usually appears at around 430 cm^{-1}.

The obtained FESEM images of the layers present on the surface of the G95/5 and G80/20 sensors using a back-scattered electron detector (BSE) shows a black layer which is the graphene layer, big grey chunks corresponding to the alumina substrate surface, and the zinc oxide nanoparticles can be detected by the bright spots. Some ZnO nanoparticles can be seen in figure 2a since the ZnO concentration in the material (G95/5) is only 5 wt.%. Meanwhile, in figure 2b, the whole surface of the layer of the G80/20 sensor is homogenously covered with ZnO nanoparticles and graphene.

The quantity and type of defects in ZnO can be estimated based on PL measurements. Figure 3 shows the PL results of the ZnO loaded graphene G95/5 sample. By pumping at 325 nm, two emission bands were observed at room temperature. A near band edge (NBE) emission in the UV at around 390 nm associated to exciton recombination processes, and a broader deep level (DL) defect emission band in the visible range from 480 to 630 nm. The DL broad emission band showed the maximum emission intensity at around 520 nm. Defects responsible for this peak at around 520 nm are related to oxygen vacancies.

3.2 Gas sensing Results

Nitrogen Dioxide (NO2) detection was performed by applying repeated exposure and recovery cycles to increasing concentrations of the gas. Figure 4 shows the calibration curves obtained for 50-250-500ppb of NO_2, in which graphene decorated with 5% of ZnO presents higher response compared to graphene decorated with 20% ZnO at room temperature. Since the G95/5 sensor was able to efficiently detect very low concentrations of NO_2, it was the subject of further measurements closer to real conditions (in other words under humidity), to check the effect of the ambient moisture on the sensor's performance. Two different relative humidity percentages of 20 and 70 % were applied, while doing the gas tests towards different concentrations of NO_2 of 50, 150, 250, 350 and 500 ppb at room temperature, the calibration curves presented in figure 5 show a quite linear behavior in the concentration range considered, allowing to determine a constant sensitivity as the slope of the regression lines.

And finally, the selectivity of the sensors was evaluated by repeating the same experimental conditions when detecting NO_2 for detecting other target gases. In this regard, 500 ppb, 25 ppm, 50 ppm, 200 ppm and 20 ppm of NO_2, CO, NH_3, Hydrogen, H_2S and Ethanol respectively were detected at room temperature under dry conditions. As can be seen in figure 6, the inclusion of the ZnO nanoparticles results in an increased response towards nitrogen dioxide gas making it selective to this specific gas.

4. Conclusions

This work reports the fabrication of a graphene-based sensor, decorated with ZnO nanoparticles using a novel and patented nanotechnological method for enhanced NO_2 sensing at room temperature. The synthesis method has been already scaled up for the mass production of gas sensitive nanomaterials (from few g up to kg). The loading of the graphene with two different percentages of ZnO has shown that the lower the loading, the better the sensing capabilities of the sensor, since the G80/20 was not capable of detecting NO_2 at concentrations lower than 250 ppb. Meanwhile, G95/5 could detect as low as 50 ppb of the target gas. Furthermore, the G95/5 sensor showed very good responses, stability, and reproducibility in the range of 50-250-500 ppb of NO_2. The sensing performance gets significantly enhanced under a humid atmosphere to reach almost 5-fold the response under a dry atmosphere, which makes it a very promising material for NO_2 detection for industrial use in farms or factories.

6. Graphs

(b)

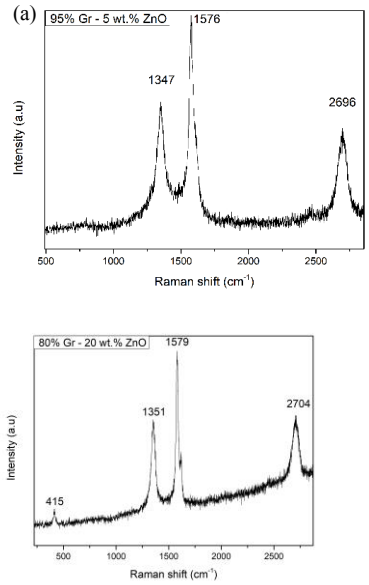

Fig.1. Raman spectrums of (a) G95/5 sensor and (b) G80/20 sensor

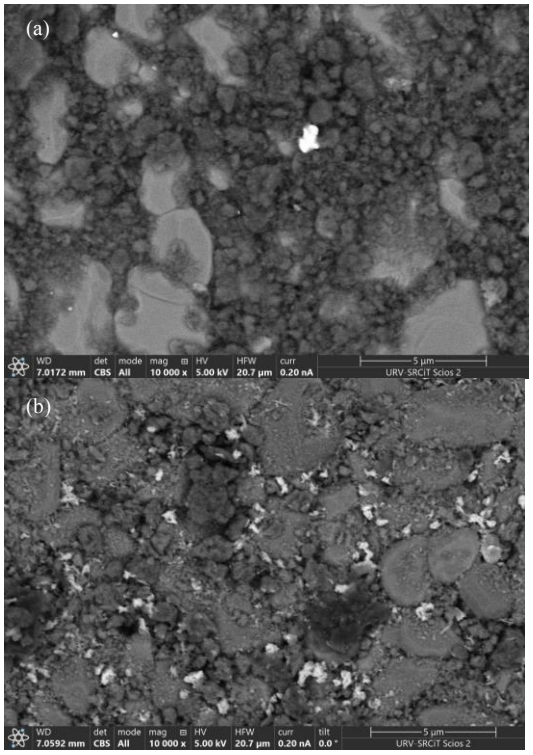

Fig.2 FESEM images of (a) G95/5 surface exhibiting few nanoparticles of ZnO (b) G80/20 showing a homogenous distribution of the ZnO nanoparticles on the surface of the layer.

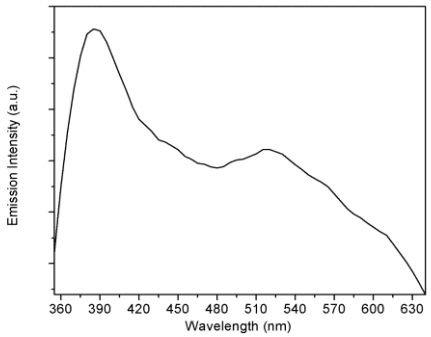

Fig.3 Photolumiscence spectra of the G95/5 sample at room temperature.

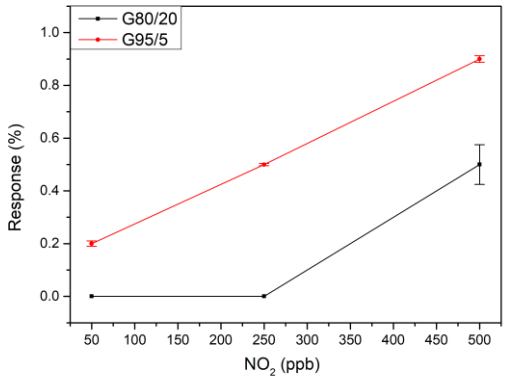

Fig.4. Calibration curves of the G95/5 (red) and G80/20 (black) sensors at room temperature for 50, 250 and 500 ppb of NO_2

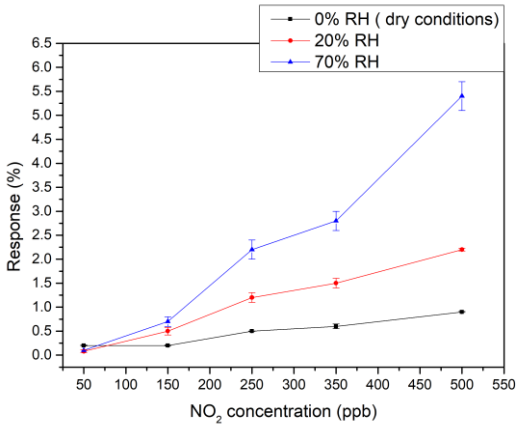

Fig.5. Calibration curves of G95/5 sensor in different relative humidity percentages: 0 (dry), 20 %, and 70 %.

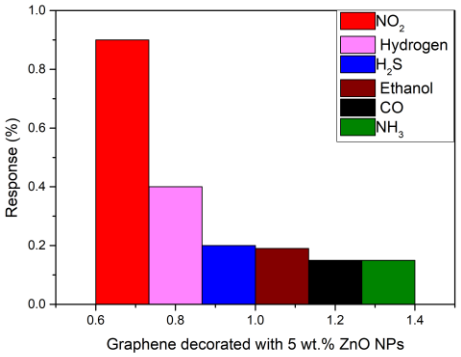

Fig.6. Comparison chart of the response of the sensors towards 500 ppb of NO_2 (red), 200 ppm of H_2 (pink), 20 ppm of H_2S (blue), 20 ppm of ethanol (brown), 25 ppm of CO (black), and 50 ppm of NH_3 (green) at room temperature and dry conditions.

Carbon dots as photoactive platforms for the photocatalytic reduction of CO_2

Beatriu Domingo Tafalla[a,*], Carla Casadevall[a,*], Emilio Palomares[a,*,♦,†]

[a]*Institute of Chemical Research of Catalonia (ICIQ), Avinguda del Països Catalans 16, 43007 Tarragona, Spain.*
Tel: +34 977 920 200; E-mail: bdomingo@iciq.es
**Universitat Rovira i Virgili (URV), N5- Edifici de Serveis Centrals Carrer Marcel·lí Domingo, 2-4-6, 43007- Tarragona*
♦*Catalan Institution for Research and Advanced Studies (ICREA), Passeig de Lluis Companys 23, 08010 Barcelona, Spain.*
†*Universidad de Pau y Pays de l'Adour (UPPA), Avenue de l'Université, 64012 Pau, Francia*
Teléfono: +33 5 59 40 70 00.

Carbon dots possess optical properties that make them suitable metal-free light absorbers for the development of hybrid systems for the photocatalytic conversion of CO_2. The surface of carbon dots can be used to anchor molecular catalysts which will ensure high activity and product selectivity. On this basis, our aim is to develop a model hybrid system in which the carbon dot functions at the same time as an anchoring scaffold and a photosensitizer of an iron porphyrin for the photoreduction of CO_2 to CO. In this work, we assess the feasibility of the formation of an hybrid system functionalizing branched polyethylenimine carbon dots using click chemistry.

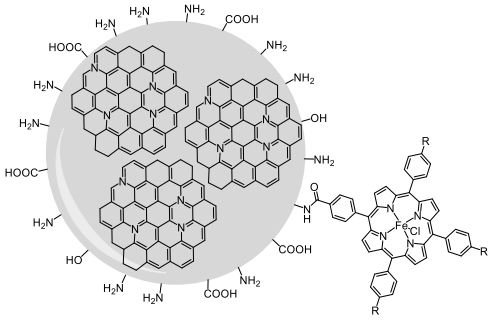

Introduction

The capture and conversion of CO_2 into value-added products are under investigation in order to counteract the increasing emissions of CO_2. A viable approach is to convert CO_2 using solar light (photocatalysis). In this regard, the most studied materials for the photoreduction of CO_2 are metal oxides, particularly, TiO_2, MgO, Ga_2O_3, Bi_2MoO_6, In_2O_3, and Ta_2O_5 [1]. However, product selectivity of heterogeneous catalysts is an issue.

As an alternative, the use of hybrid systems that combine a photoabsorber and a molecular catalyst selective for a specific product has gained attention. Carbon dots (CDs), with easy large-scale production, high chemical stability and excellent photo/electro properties are promising candidates for the design of this kind of hybrid systems [2]. Their highly functionalized surface can serve as a platform for covalent anchoring of molecular catalysts.

In this work, the feasibility of the production of an hybrid photocatalyst based on branched polyethylenimine (BPEI) CDs is investigated. BPEI CDs are easily produced by hydrothermal synthesis methods and are further functionalized via click reaction method.

Methodology

Synthesis of surface functionalized amorphous carbon dots (CDs)

Amorphous CDs were synthesized with a bottom-up approach from carbon and nitrogen containing precursors following a previously reported procedure [3]. Briefly, 0.6 g of branched polyethylenimine (M.W. 1800) and 1 g of citric acid were dissolved in 10 mL boiling water and then stirred under reflux for 3 hours. The color of the solution changed from transparent to yellow confirming the formation of the CDs, which were further purified by silica gel column chromatography with 0.01 M HCl solution as the developing solvent. In order to eliminate polyethylenimine remains, the CDs solution was further filtered through 0.2 µm syringe cellulose filters. Dry CDs were obtained by freeze drying.

Integration of the hybrid system

P-anisidine was covalently anchored to the surface of CDs following a previously reported procedure [1]. Briefly, 100 mg of CDs were dissolved and reacted with 8 mL of thionyl chloride under inert conditions at 80 C for 24 h in order to activate the carboxylic acid group of the CDs. After cooling down to 40 C, the remaining $SOCl_2$ was removed by evaporation and by three successive cycles of dissolution in dry THF followed by evaporation. Then, 100 mg of p-anisidine dissolved in 5 mL of dry DCM with 10 $\%_{w/w}$ etilamine were added and the solution was stirred under argon for 48 h at room temperature. Finally, the solvent was rotaevaporated and the black solid was washed with diethyl ether to yield CD@p-anisidine.

Results

Obtention of CDs and CD@p-anisidine

CDs were obtained as a water soluble white solid. Contrarily, CD@p-anisidin were obtained as a water

insoluble brown solid, soluble in polar organic solvents such as methanol or DMSO.

Characterization of CDs

Fourier transform infrared spectroscopy (FT-IR) verifies the presence of functional groups on the surface of CDs (Fig. 1A). The broad band in the range of 3300-3500 cm^{-1} is attributed to primary and secondary amines, while the sharp band at 1705 cm^{-1} indicates the presence of -COOH. X-Ray pattern (Fig. 1B) shows a broad peak at $2\theta = 40^{\circ}$ and the absence of the graphitic peak at $2\theta = 26.5^{\circ}$, confirming the amorphous structure of CDs. The absence of D and G bands in the Raman spectra also accounts for this fact. 1H-NMR spectrum (Fig. 2) shows two doublets between 2.6 and 3.0 ppm assigned to olefine bonds and no bands in the aromatic region. The elemental composition of the CDs, determined by elemental analysis, is 7.09 % of nitrogen, 39.61 % of carbon, 5.79 % of hydrogen and 47.52 % of oxygen. X-Ray Photoelectron Spectroscopy (XPS) analysis have been performed to confirm the functionalization of the CDs. Deconvolution of the N1s peak (Fig. 1C) confirms the presence of primary (400.15 eV) and secondary (399.01 eV) amine groups, which are related to the C1s deconvoluted peaks at 285.85 eV and 288.36 eV. Deconvolution of the O1s peak confirms the presence of C=O (531.72 eV) and C-O-H (533.07 eV) bonds.

UV-Vis absorbance spectra of an aqueous solution of CDs (Fig. 1D) shows a unique absorption peak at 358 nm assigned to n-π* transitions from surface functional groups. Under light excitation in the range of 318-418 nm, CDs exhibit a slight excitation dependent emission with a maximum at 445 nm of emission wavelength upon 358 nm excitation. Transmission electron microscopy (TEM) images (Fig. 1F) show a particle diameter in the range of 3 to 6 nm.

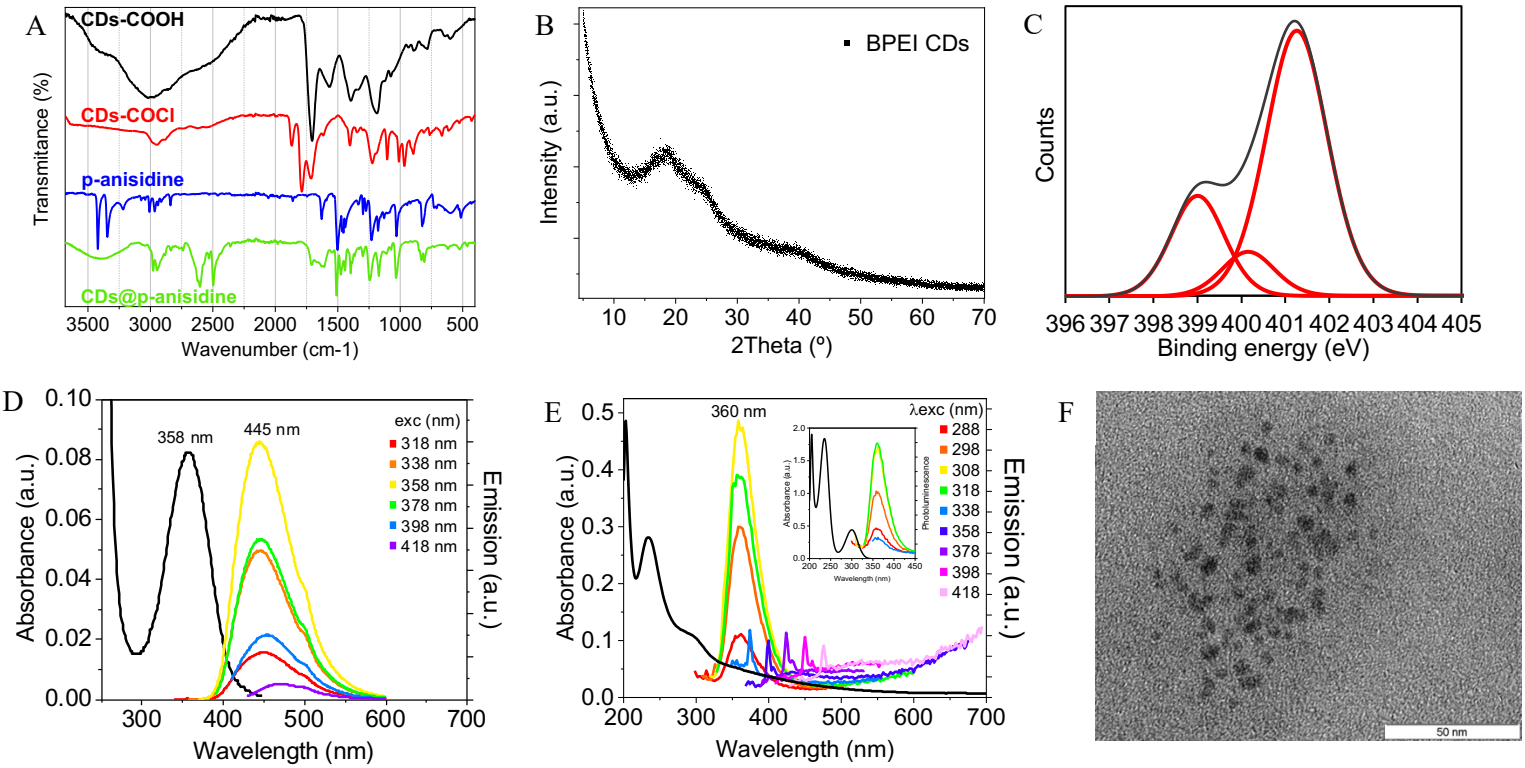

Figure 1. FT-IR (A), powder XRD (B) and XPS-N1s (C) spectra of solid CDs. UV-Vis absorbance and emission spectrum of a 5 mg/mL aqueous solution of CDs (D) and of a methanol solution of CDs@p-anisidine. TEM image of CDs (F).

Characterization of the CD@p-anisidine hybrid

FT-IR confirms partial transformation of the carboxylic acid on the surface of CDs to acyl chloride, according to the -C=O band at 1800 cm^{-1} (Fig. 1A). FT-IR also confirms the presence of p-anisidine on the surface of CDs. The doublet at 1660 cm^{-1} (C=O stretch) and at 1546 cm^{-1} (N–H bending) is attributed to the amide bond between CDs and p-anisidine. The bands at 1090 cm^{-1} and 3000 cm^{-1} are attributed to the methoxy group and aromatic bonds of the p-anisidine, respectively. The broad band in the 3300-3000 cm^{-1} region is attributed to the -N-H stretching of the amide bond. In the same region, the doublet of the primary amine of the p-anisidine is not observed, confirming the formation of

the amide bond. 1H-NMR spectrum of CD@p-anisidine shows the aromatic signals of the p-anisidine ring in the 6.4-6.7 ppm range, slightly shifted with respect to p-anisidine (Fig. 2).

UV-Vis absorbance spectra of a methanol solution of CD@p-anisidine shows a band at 235 nm and a broad shoulder at 300 nm that resemble the absorbance of p-anisidin (inset in Fig. 1E). An absorbance tail that extends until 550 nm accounts for the absorbance of CDs. CD@p-anisidine present emission features of both CDs and p-anisidine. The strong and slightly excitation dependent emission centered at 360 nm resembles the strong excitation independent emission of p-anisidine (inset in Fig. 1E), while the weak emission in the range of 450 nm to 550 nm arises from the CDs themselves (sharp peaks in this region are due to the Raman signal of the methanol solvent).

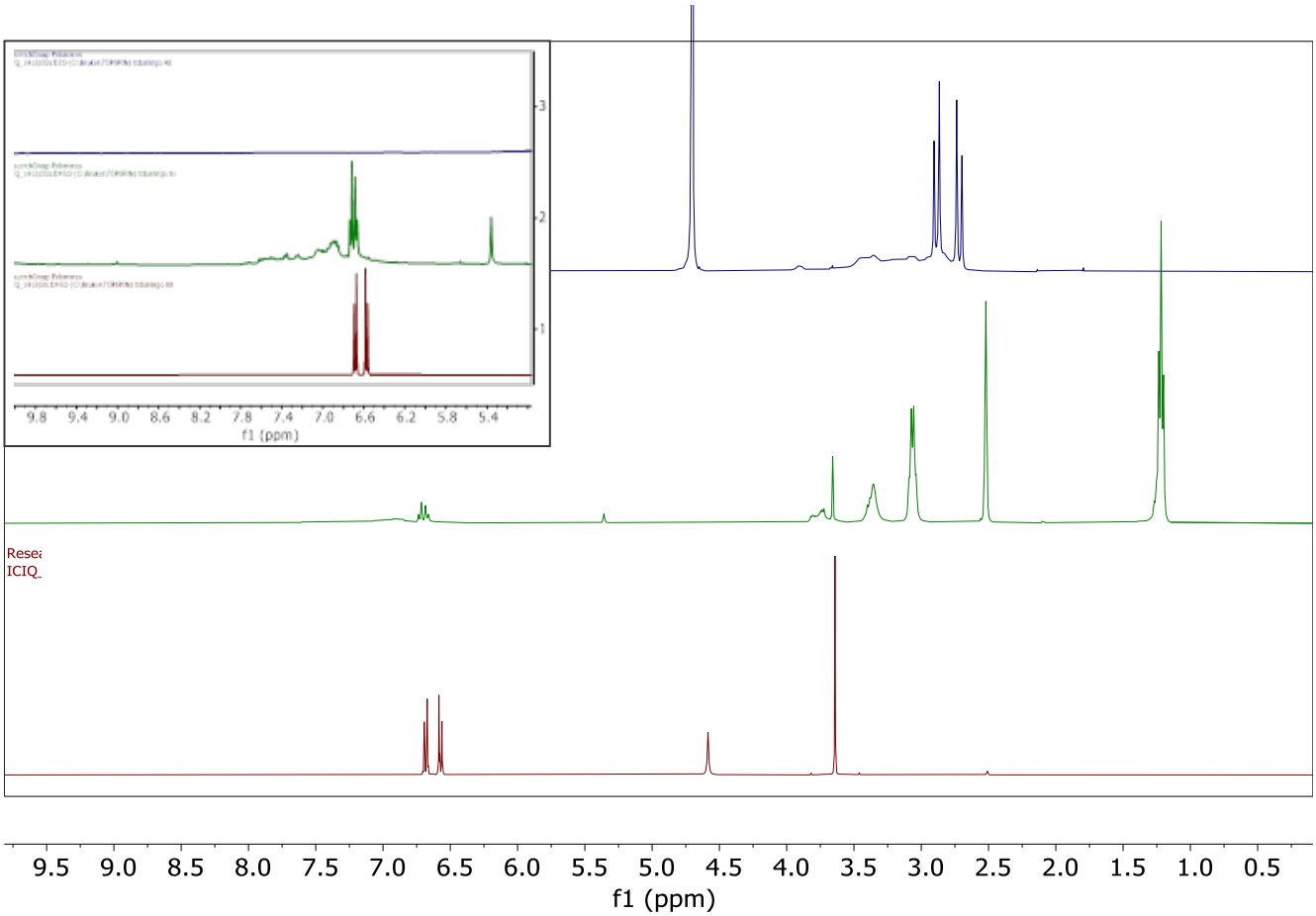

Figure 2. 1H-NMR spectrum of CDs in D_2O (blue), CD@p-anisidine in dDMSO (green) and of p-anisidine in dDMSO (red). The inset spectrum is the aromatic region.

Conclusions and future work

Amorphous CDs obtained from the hydrothermal treatment of BPEI polymer and citric acid were functionalized with p-anisidine through amide bond using a click chemistry method. Therefore, the feasibility of the covalent functionalization of has been confirmed. The subsequent step will be to functionalize these CDs with a tetraphenyl porphyrin bearing an amine group following the same approach.

Bibliography

[1] A. Call *et al.*, "Improved electro-and photocatalytic water reduction by confined cobalt catalysts in streptavidin," *ACS Catal.*, vol. 9, no. 7, pp. 5837–5846, 2019.

[2] L. Đorđević, F. Arcudi, and M. Prato, "Preparation, functionalization and characterization of engineered carbon nanodots," *Nat. Protoc.*, vol. 14, no. 10, pp. 2931–2953, 2019.

[3] Z. Zhang *et al.*, "Quinoline derivative-functionalized carbon dots as a fluorescent nanosensor for sensing and intracellular imaging of Zn2+," *J. Mater. Chem. B*, vol. 2, no. 31, pp. 5020–5027, 2014, doi: 10.1039/c4tb00677a.

Hybrid Structures Based on Nanoporous Anodic Alumina for Optical Detection of Alcohol–Containing Fluids

Alejandro Rojas Gómez[1], Laura K. Acosta[1], Josep Ferré–Borrull[1], Abel Santos[2,3*], and Lluis F. Marsal[*1]

[1]Department of Electronic, Electric, and Automatics Engineering, Rovira i Virgili University, Tarragona 43007, Spain
[2]School of Chemical Engineering and Advanced Materials, The University of Adelaide, South Australia, 5005, Australia
[3]Institute for Photonics and Advanced Sensing, The University of Adelaide, South Australia, 5005, Australia
*E–mails: abel.santos@adelaide.edu.au; lluis.marsal@urv.cat

Abstract

Hybrid metal/dielectric nanostructures has inspired the use of Tamm plasmon resonance in the design of optical detection systems. In this work, we fabricated gradient-index filters based on nanoporous anodic alumina (GIF–NAA) using the pulse-like anodization technique and coated the fabricated samples with gold using the sputtering technique. This material combines one-dimensional photonic crystal made of aluminium oxide (dielectric) with a plasmonic material (metal). Its sensing capabilities were examined by using reflectometric interference spectroscopy (RifS). The experiments were developed in a flow cell in real time by infiltrating various alcoholic fluids into the nanopores. Results highlight the application of this platform for optical sensing of volatile compounds.

1. Introduction

Tamm plasmon resonances first proposed by Kaliteevski and co-workers are a class of surface plasmons in which incident light is confined at the interface of a hybrid structure consisting of a thin metallic coating layer (e.g., Au, Ag, Pt) and a dielectric mirror (e.g., Bragg reflector) [1].

One of the most interesting aspects of Tamm plasmons is that resonant photons confined at and travelling along the plasmonic–photonic interface are highly susceptible to changes in the refractive index of the surrounding medium [2]. As such, the resonance band of the Tamm plasmon system undergoes a spectral shift, which is proportional to the change of refractive index. This property in turn can be readily harnessed as the core principle to develop highly sensitive sensing systems [3,4].

Recently, nanoporous anodic alumina photonic crystals (NAA–PCs) produced by pulse-like anodization of aluminum have been demonstrated as suitable platforms to develop Tamm plasmon sensors [5].

In this study, we use the reflectometric interference spectroscopy (RifS) technique to elucidate the sensing capabilities of our samples (Au–coated GIF–NAA), by monitoring the Tamm plasmon resonance in surface adsorption experiments using. The experiments were developed in a flow cell in real time by infiltrating various alcoholic fluids into the nanopores. The results highlight the application of Au–coated GIF–NAA as a potential platform for optical sensing of volatile organic compounds by monitoring the Tamm plasmon resonance.

2. Fabrication of Au–Coated NAA–GIF

Aluminum sheets were cut into squared chips with a side of 2 cm. The surface of as-received Al chips was cleaned sequentially with acetone, water and ethanol to remove impurities before starting the fabrication process. The surface of cleaned Al chips was smoothened by electropolishing in a mixture electrolyte solution of 4:1 v/v ethanol–perchloric acid at 20 V and 5 °C for 8 min. During this process, the direction of stirring was alternated every 60 s. After electropolishing, Al chips were anodized by sinusoidal pulse anodization in a 0.3 M oxalic acid electrolyte at 5 °C. Current density sinusoidal anodization profiles were generated in a LabView customized application, following Equation 1:

$$J(t) = J_{max} \sin\left(\frac{2\pi}{T} t\right) + J_{offset}$$

$$\text{for } 0 < t < N \cdot T \qquad (1)$$

where $J(t)$ is the applied current density (in mA cm^{-2}) at time t (in seconds), J_{offset} is the offset of the current density during the anodization process, J_{max} is the maximum of current density in absolute value with respect to its average, T is the anodization period of the sinusoidal profile (in seconds), which represents the time difference between consecutive pulses, and N is the number of sinusoidal pulses in the anodization profile.

The values of J_{offset}, J_{max} and N were fixed to 2 mA cm^{-2}, 1 mA cm^{-2}, and 120 pulses respectively, whereas the input anodization period was set to T = 240 s, to produce NAA–GIFs with PSBs located at a specific position of the visible region of the electromagnetic spectrum.

A layer of gold with controlled thickness was deposited on the top surface of these NAA-based PC structures by sputtering technique by controlling the sputtering time. Preliminary calibration experiments revealed a gold coating layer thickness of 23 ± 1 nm at 60 s of deposition time under the conditions used in our system (30 mA).

3. Results and discussions

The sensing principle was demonstrated by infiltrating four different alcohols inside the nanopores of the created hybrid structure, in increasing order of the respective refractive index (ethanol, 2-propanol, methyl-2-propanol and ethane-1,2-diol, respectively). Alcohols are physically adsorbed on the entire surface in a process governed by diffusion into the pores. In the experiments, a fluid rate of 30 was used and every 10 min the alcoholic fluid that was passed through the sample in the fluid cell was changed.

Real time monitoring by RifS measurements showed a redshif for λ_{Tamm} with increasing the refractive index of infiltrated alcohol (Fig.1). The variation of the Tamm resonance with the refractive index of alcohol showed a linear behavior throughout the range of refractive indices considered (R = 0.997).

The sensitivity shown was 28.4 nm/RIU but we believe that it can be improved much more. As-produced NAA-based GIFs feature Tamm resonances after coating their top surface with non–continuos gold layers. However, the quality of light confinement is assumed to get progressively worse with the porous gold coating layer thickness after a critical value. This constraint can be addressed by widening the nanoporous structure and broadening its characteristic photonic stopband [6]. So, if we engineer the structure and modify the porosity of the samples in combination with less gold coating, we can find some optimized parameters for developing new experiments with extra sensitivity. Even so, it should be noted that the fabricated samples can perfectly discriminate pure alcohols with a difference in refractive index of 35 thousandths or less. The experiments can be extended using aqueous solutions of each of these alcohols and the sensitivity of the detection system to each of them can be studied separately.

4. Conclusions

In summary, this work demonstrates that sinusoidal pulse-like anodization approach in combination with sputtering makes it possible the generation of Au-coated NAA–GIFs as a model hybrid metal–dielectric platform with narrow photonic stopband and Tamm plasmon resonances within specific position of the visible electromagnetic spectrum.

Upon coating, Tamm plasmon resonances were observed in the reflectance spectra of these structures.

The results highlight the application of Au–coated GIF–NAA as a potential platform for optical sensing of volatile organic compounds by monitoring the Tamm plasmon resonance.

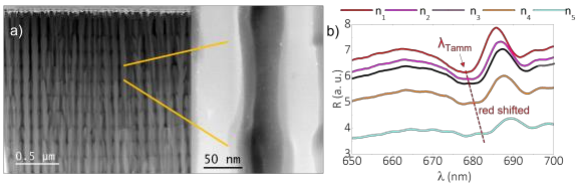

Fig.1. a) Cross–section TEM image of Au–coated GIF–NAA with magnified view of the sinusoidal nanopore created through pulse-like anodization nanofabrication technique with sinusoidal current density profile; b) Minimum wavelength in reflectance spectrum corresponding to the Tamm plasmon resonance (λ_{Tamm}) is red shifted by infiltrating fluids into the nanopores created in increasing order of refractive index.

Acknowledgments:

This work was supported by the Spanish Ministerio de Ciencia e Innovación (MICINN/FEDER) PDI2021-128342OB-I00, by the Agency for Management of University and Research Grants (AGAUR) ref. 2021-SGR-00739, by the Diputació de Tarragona (DIPTA) 2022/33, and by the Catalan Institution for Research and Advanced Studies (ICREA) under the ICREA Academia Award. Prof. Abel Santos thanks the support provided by the Australian Research Council through the grants DP200102614 and DP220102857.

References

[1] H. N. Q. Tran, N. D. A. Le, Q. N. Le, C. S. Lim, S. Y. Law, A. D. Abell, A. Santos, "Spectral Engineering of Tamm Plasmon Resonances in Dielectric Nanoporous Photonic Crystal Sensors", *ACS Applied Materials and Interfaces*. American Chemical Society, pp 22747–22761, May 25, 2022.

[2] W. L. Barnes, A. Dereux, T. W. Ebbesen, "*Surface Plasmon Subwavelength Optics"*; www.nature.com/nature, 2003.

[3] I. Abdulhalim, M. Zourob, A. Lakhtakia, "Surface Plasmon Resonance for Biosensing: A Mini-Review". *Electromagnetics,* 28 (3), 214–242, 2008.

[4] A. Juneau-Fecteau, R. Savin, A. Boucherif, L. G. Fréchette, "A Practical Tamm Plasmon Sensor Based on Porous Si", *AIP Adv* 11 (6), 2021.

[5] C. S. Law, L. F. Marsal, A. Santos, "Electrochemically Engineered Nanoporous Photonic Crystal Structures for Optical Sensing and Biosensing". In Handbook of Nanomaterials in Analytical Chemistry: Modern Trends in Analysis; Elsevier, pp 201–226, 2019.

[6] A. Rojas Gómez, L. K. Acosta, J. Ferré-Borrull, A. Santos, and L. F. Marsal, "Generation of Tamm Plasmon Resonances for Light Confinement Applications in Narrowband Gradient-Index Filters Based on Nanoporous Anodic Alumina", ACS Applied Nano Materials, *6* (7), pp 5274-5283, 2023.

Copper-based hybrid nanomaterials for the electrocatalytic reduction of CO_2

Joan Marc Bondia Pedra [a, b], Federico Franco [a], Carlos Puerto [a], Emilio Palomares-Gil [a, c]

[a] *Institute of Chemical Research of Catalonia (ICIQ), The Barcelona Institute of Science and Technology, Tarragona 43007, Spain*
[b] *Departament d'Enginyeria Electrònica, Elèctrica i Automàtica, Universitat Rovira i Virgili, Avinguda dels Països Catalans, 26, Tarragona, Spain*
[c] *ICREA, Passeig LLuis Companys 23, E-08010, Spain*

Abstract

In the perspective of drastically reducing anthropogenic CO_2 emissions, the electrochemical CO_2 reduction reaction (CO_2RR) powered by renewable energy sources and catalyzed by transition metal-based catalyst has become an attractive sustainable approach to tackle this challenge. Among the plethora catalysts, Copper (Cu)-based nanocatalyst have attracted increasing interest in the field over the last decades, due to their unique capability to promote an electrochemical reduction of CO_2 into multicarbon C_{2+} products.
In this work, we developed hybrid molecular-heterogeneous Cu-based nanomaterials for CO_2RR, with the aim of tuning the selectivity of the nanostructured Cu catalyst by the combination with a molecularly defined polymeric matrix. The resulting hybrid materials showed a clear trend in which C_1 products, especially methane (CH_4) and formate ($CHOO^-$), are favored versus the formation of C_{2+} products (FE_{CH4} = 25% at -1.10V vs RHE).

1. Introduction

Global warming, worldwide energy crisis and the issues related to increasing levels of carbon dioxide (CO_2) have prompted the research of new catalysts to transform CO_2 back to fuels and value-added chemicals[1]. New technologies have been implemented to convert CO_2 to carbonaceous fuels and commodity chemicals, such as methane, ethylene, and ethanol among others, powered by renewable sources to achieve a new green economy[2]. Although several transition metal-based systems have been reported to catalyze the CO_2 reduction reaction[3] (CO_2RR), catalyst selectivity and durability still represents major challenges to achieve an efficient CO_2RR, mainly due to catalyst deactivation and to competitive Hydrogen evolution reaction (HER) and/or alternative pathways leading into multiple carbon-based products. However, the combination of molecules (both organic modifiers and organometallic complexes) and nanostructured materials has recently revealed to be an effective strategy to improve overall efficiency and selectivity of the CO_2RR process[4]. In particular, the formation of hybrid catalysis based on the integration of organic molecules or reticular frameworks with heterogeneous metal or metal-oxide surfaces allowed to tune stability of key intermediates or the local environment of the catalysts, resulting in a significant improvement of the CO_2RR[5].

In this contribution, Cu_2O nanocubes (NCs) are used as both templates and catalysts for an in-situ polymerization based on a Cu-catalyzed azide-alkyne cycloaddition reaction (CuAAC) in the presence of the corresponding monomeric building blocks[6] (Figure 1). This approach results in a series of hybrid nanoreactors with well-defined shape and size, which are active electrocatalysts for CO_2 reduction in neutral pH.

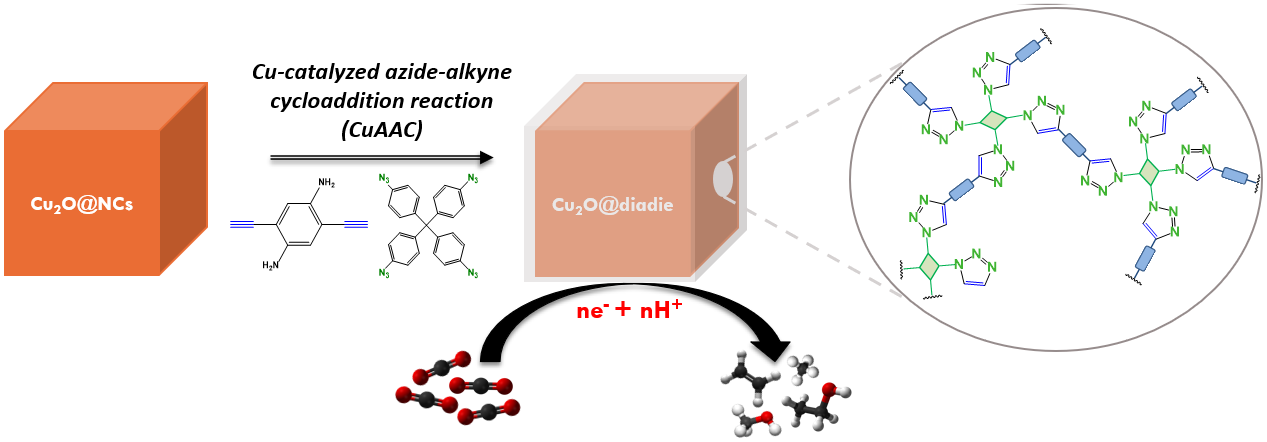

Figure 1. Scheme of the catalyst design: Cu_2O nanocubes catalyzing the in-situ azide-alkyne cycloaddition reaction between the monomeric building blocks to form the Cu_2O@diadie hybrid nanocatalyst with an organic coating for CO_2 reduction.

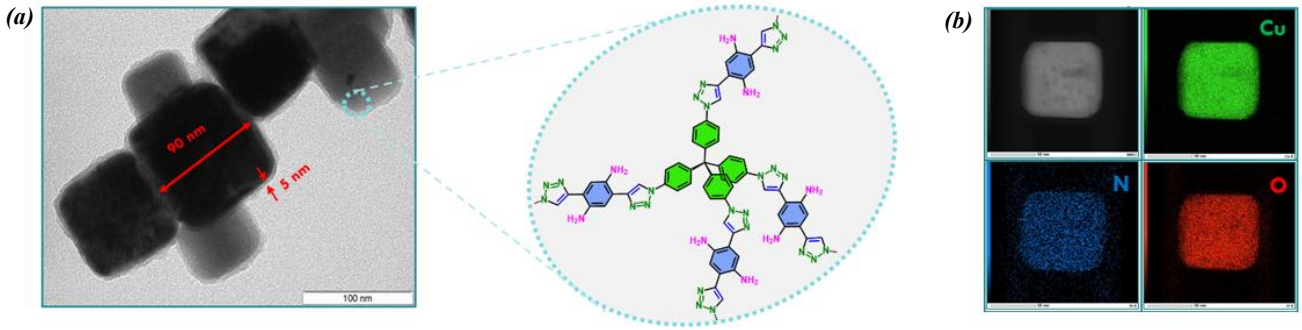

Figure 2. *a) TEM images of Cu_2O@diadie hybrid nanoreactors and b) EDX mapping of Cu_2O@diadie hybrid nanoreactors.*

2. Results and discussions

To confirm the formation of the organic coating layer and the retention of the size and structure of Cu_2O NCs, microscopic and spectroscopic technics were used to characterize the hybrid nanoreactors. Transmission electron microscopy (TEM) images show the retention of the average size (90 nm) and the cubic shape of Cu_2O nanocubes after the click cycloaddition, confirming the robustness of the reaction (Figure 2a). Additionally, an organic coating can be observed with an average thickness of 5nm, forming the desired hybrid nanomaterial, which is confirmed by TEM-EDX (Figure 2a,b). N, Cu and O mappings give evidence of the formation of an organic layer wrapping the Cu_2O nanocubes (Figure 2b). Powder X-Ray diffraction (PXRD) results of bare Cu_2O nanocubes showed peaks at 29.6, 36.4, 42.3, 61.4, 73.6 and 77.4º of 2θ values, which corresponds to (110), (111), (200), (220), (311), and (222) diffraction planes. This pattern closely matches with both, the characteristic pattern of crystalline cubic Cu_2O and the pattern of the hybrid material (Cu_2O@diadie) (Figure 3b). Attenuated total reflectance-Fourier transformed infrared (ATR-FTIR) results reveal the characteristic vibrational peak at 600 cm^{-1} which corresponds to the stretching vibration of Cu-O bond coming from pure Cu_2O, indicating the retention of the copper oxide (I) structure. Moreover, the absence of azide and alkyne peaks (at 2100 and 3128 cm^{-1} respectively) and the appearance of the bands at 1600 cm^{-1} corresponding to triazole moieties confirms the formation of the coating polymer (Figure 3a).

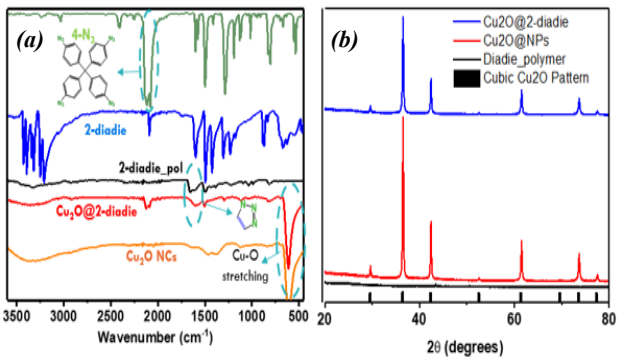

Figure 3. a) ATR-FTIR spectra and b) PXRD spectra of Cu2O@diadie, bare Cu2O NCs, and diadie polymer.

The Cu_2O hybrid materials have been tested to be effective catalysts for the efficient electrochemical reduction of CO_2, leading to a mixture of C_1 and C_{2+} products. Both bare Cu_2O NCs and Cu_2O@diadie nanoparticles, follow the potential-dependent selectivity where the formation of CO, H_2, and $CHOO^-$ are favored at low overpotentials, whereas at high overpotentials, C_{2+} products (mainly C_2H_4 and C_2H_6O) are formed (Figure 4a,b). However, the surrounding polymer on the Cu_2O@diadie nanoreactors seems to have a clear effect in selectivity, slightly increasing the FE of C_1 products at high overpotentials (FE = 25% of CH_4 over 10% at -1.10V vs RHE). Furthermore, another trend can be observed regarding H_2 formation. At low overpotential, the FE of H_2 is higher for Cu_2O@diadie compared to bare Cu_2O NCs (FE_{H2}= 70% over 33% at -0.8V vs RHE). Nevertheless, at high overpotentials the FE of H_2 decreases for Cu_2O@diadie whereas the formation of H_2 for Cu_2O NCs increases (FE_{H2} = 31%

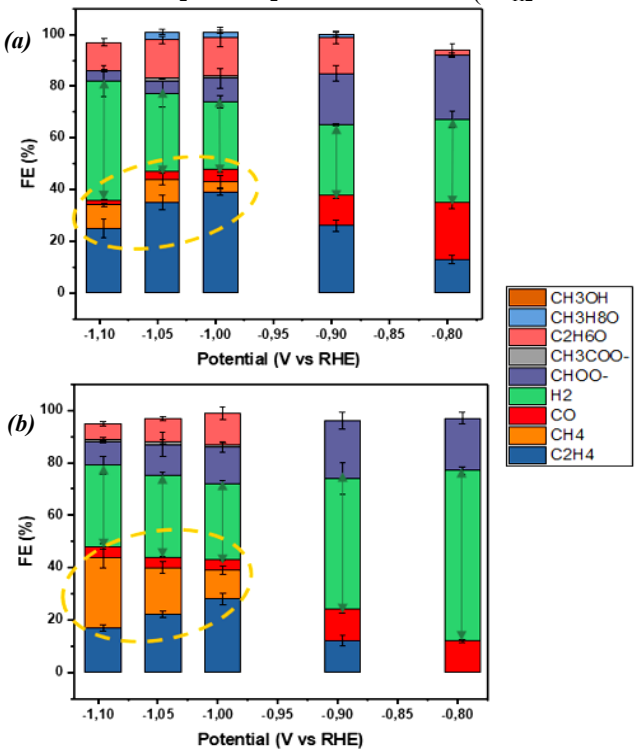

Figure 4. a) FE of bare Cu_2O NCs and b) FE of Cu_2O@diadie nanocubes

over 45% at -1.10V vs RHE) (Figure 4b).

3. Conclusions

The study presents an innovative method for the rational design of hybrid heterogeneous-molecular Cu-based nanomaterials for CO_2RR, using well defined Cu_2O nanocubes as reference system. The formation of the polymeric coating wrapping the Cu_2O nanoparticles, which were used as template and catalyst, as well as the structural retention of the original Cu_2O nanocubes, were successfully confirmed by using spectroscopic and microscopic techniques. Regarding catalysis, the bare Cu_2O and the hybrid Cu_2O@diadie nanoreactors found to be competent electrocatalysts for CO_2RR in a neutral pH electrolyte following a similar analogous trend. Unlike the bare Cu_2O NCs, the hybrid Cu_2O@diadie nanocubes display unique features in selectivity, slightly increasing the FE of C_1 products at high overpotentials and decreasing the FE of H_2 at high overpotentials.

4. References

[1] Franco, F.; Rettenmaier, C.; Jeon, H. S.; Cuenya, B. Transition metal-based electrochemical CO2 reduction: from atoms and molecules to nanostructured materials. Chem. Soc. Adv., 2020, 49, 6884.

[2] Kuhi, K. P.; Cave, E. R.; Abram, D. N.; Jaramillo, T. F. New insights into the electrochemical reduction of carbon dioxide on metallic copper surfaces. Energy Environ. Sci., 2012, 7050-7059.

[3] Domingo-Tafalla, B.; Martínez-Ferrero, E.; Franco, F.; Palomares-Gil, E.; Applications of Carbon Dots for the Photocatalytic and Electrocatalytic Reduction of CO2, Molecules 2022, 27, 108.

[4] Nam , D.-H.; De Luna, P.; Rosas-Hernández , A.; Thevenon, A.; Li, F.; Agapie, T.; Peters, J. C.; Shekhah, O.; Eddaoudi, M.; Sargent, E. H.; Nature Materials 2020, 19, 266.

[5] Thevenon, A.; Rosas-Hernández, A.; Peters, J. C.; Agapie, T.; In-Situ Nanostructuring and Stabilization of Polycrystalline Copper by an Organic Salt Additive Promotes Electrocatalytic CO2 Reduction to Ethylene, Angew. Chem. 2019, 131, 17108.

[6] Chassaing, S.; Bénéteaub, V.; Pale, P.; When CuAAC 'Click Chemistry' goes heterogeneous, Catal. Sci. Technol., 2016, 6, 923.